Supplementary Information

Theoretical studies on anhydride dynamic covalent bond exchange mechanisms

Xinglong Zhang,[1,2,] * Qiubo Chen,[1] Nannan Li,[1] Michael B. Sullivan,[1] Jianwei Zheng[1,] *

[1]Institute of High Performance Computing, Agency for Science, Technology and Research (A*STAR), 1 Fusionopolis Way, #16-16, Connexis, Singapore 138632, Singapore

[2]Department of Chemistry, The Chinese University of Hong Kong, Shatin, New Territories, Hong Kong, China

Email: xinglong.zhang@cuhk.edu.hk; zhengjw@a-star.edu.sg

Table of Contents

I. Computational Methods

I.1 Benchmarking of prototypical system

For the study of the mechanism of the prototypical system of anhydride exchange between methacrylic anhydride (MAA) and 4-pentenoic anhydride (PNA) molecules, the global hybrid DFT functional M06-2X[1] was employed. To test the effect of basis sets, the geometry optimization were performed in the gas phase separately with the Karlsruhe-family double-ζ valence def2-SVP[2,3] basis set for all atoms or with the Pople-type split-valence, singly diffuse basis set 6-31+G(d).[4] For the M06-2X/def-SVP gas phase optimised structures, single point (SP) corrections were performed using M06-2X functional and def2-TZVP[2,3] basis set for all atoms. For the M06-2X/6-31+G(d) gas phase optimised structures, SP corrections were performed using M06-2X functional and 6-311++G(d,p)[4] basis set for all atoms. For each of these SP calculations, the implicit SMD continuum solvation model[5] for chloroform ($CHCl_3$) solvent was used to account for the effect of solvent on the potential energy surface (PES). For a third method, geometry optimizations were carried out directly in implicit SMD solvent chloroform at M06-2X/def-SVP level of theory, followed by the SP correction in implicit SMD solvent chloroform at M06-2X/def-TZVP level of theory. In summary, three different levels of theories were tested: SMD($CHCl_3$)-M06-2X/def2-TZVP//M06-2X/def-SVP, SMD($CHCl_3$)-M06-2X/6-311++G(d,p)//M06-2X/6-31+G(d), SMD($CHCl_3$)-M06-2X/def2-TZVP//SMD($CHCl_3$)-M06-2X/def-SVP. These calculations were performed with *Gaussian 16* rev. B.01 software.[6]

Additionally, for the SP calculation on the gas phase optimised geometry at M06-2X/def-SVP level of theory, we performed the domain-based local pair natural orbital – coupled cluster with perturbative triple excitations (DLPNO-CCSD(T)) calculations[7,8] using ORCA version 5.0.4[9–11]. T_0 approximation which neglects the couplings between different triples by the off-diagonal Fock matrix elements, instead of the recently published iterative T_1 algorithm[12], was employed. The NormalPNO settings with $T_{cutPairs} = 10^{-4}$, $T_{CutDO} = 10^{-2}$, $T_{CutPNO} = 3.33\times10^{-7}$ and $T_{CutMKN} = 10^{-3}$ was used throughout. The TightSCF convergence with KDIIS algorithm[13] for SCF iterations were used. The complete basis set (CBS) extrapolation scheme of Helgaker et al.[14–16] using correlation-consistent double-/triple-ζ cc-pV(DT)Z basis set.[17–19] The auxiliary basis sets required for the integral evaluations in the DLPNO-CCSD(T) correlation energy calculations were generated automatically using the "AutoAux" command from the automated auxiliary basis set construction module[20] of ORCA. DEFGRID3 grid for integration was employed throughout.

For the extrapolation to complete basis set, the obtained values from cc-pVDZ basis set and from cc-pVTZ basis set are extrapolated according to the following formulae:

$$E_{\text{SCF}}^{(X)} = E_{\text{SCF}}^{(\infty)} + A \exp(-\alpha\sqrt{X}) \qquad \text{Eq (1)}$$

$$E_{corr}^{(\infty)} = \frac{X^\beta E_{\text{corr}}^{(X)} - Y^\beta E_{\text{corr}}^{(Y)}}{X^\beta - Y^\beta} \qquad \text{Eq (2)}$$

for the extrapolation of HF energy (Eq (1)) and of correlation energy (Eq (2)) to the basis set limit, respectively. $E^{(X)}_{SCF/corr}$ is the SCF/correlation energy calculated with basis set of cardinal number X, and $E^{(\infty)}_{SCF/corr}$ is the basis set limit SCF/correlation energy and A, α, and β are constants. For correlation energy, X and Y are the cardinal numbers of the basis sets used for extrapolation (X=2, Y=3 herein). For Extrapolate(2/3, cc), α=4.42 (SCF extrapolation), and β=2.46 (correlation extrapolation).

All structural and molecular orbital visualisations were performed using the open-source PyMOL[21] software.

II. Mechanism of dynamic covalent bond exchange between methacrylic anhydride (MAA) and 4-pentenoic anhydride (PNA)

Supplementary Scheme 1 shows the model reaction for the anhydride covalent bond exchange between methacrylic anhydride (MAA) and 4-pentenoic anhydride (PNA) used in our computational studies. This reaction has experimentally measured kinetic values using ^{13}C NMR spectroscopy in deuterated chloroform solvent, CDCl$_3$, for the anhydride dynamic covalent bond exchange.[22]

methacrylic anhydride
(MAA)

4-pentenoic anhydride
(PNA)
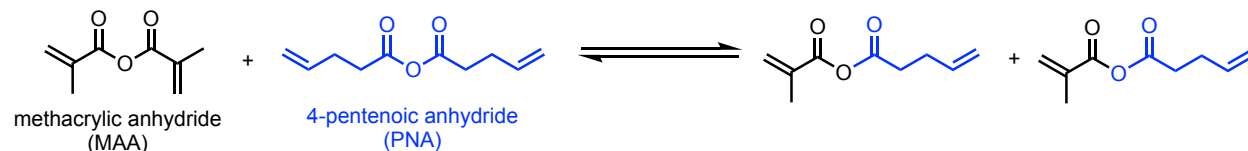
Supplementary Scheme 1. Model reaction for anhydride covalent bond exchange between methacrylic anhydride and 4-pentenoic anhydride.

II.1 Preliminary DFT benchmarking

Preliminary mechanistic studies located the 4-membered transition states (TSs) (Scheme 2ii, pathway b) and these are then used for benchmarking the different DFT bases on their effect on the PES. In studying this pathway, we kept all relative conformations and orientations of side groups consistent throughout. Note that although we later found a more favourable pathway via 6-membered TSs (Scheme 2ii, pathway a), for the purpose of initial benchmarking of DFT levels of theory, it is sufficient to consider any reaction pathway.

Four levels of theory were chosen for comparison: 1) SMD(CHCl$_3$)-M06-2X/def2-TZVP//M06-2X/def2-SVP; 2) SMD(CHCl$_3$)-M06-2X/def2-TZVP//SMD(CHCl$_3$)-M06-2X/def2-SVP; 3) SMD(CHCl$_3$)-M06-2X/6-311++G(d,p)//M06-2X/6-31+G(d) and 4) SMD(CHCl$_3$)-DLPNO-CCSD(T)/CBS(complete basis set, cc-pVDZ, cc-pVTZ)//M06-2X/def2-SVP. We adopt the conventional DFT notation in which the separator "//" is used to separate the level of theory for geometry optimization that comes after it, and the level of theory for high-level single-point energy correction (usually together with implicit solvation model) that comes before it. A single "/" separator separates DFT functional that comes before it and basis set that comes after it. In comparing levels 1 and 2, we aim to discern if there is any effect using the geometry optimised in

the gas phase versus optimised in the solvent phase. In comparing levels 1 and 3, we aim to see if there is any effect of using different basis sets, namely the more modern Karlsruhe basis sets (def2-family) [2,3] vs. Pople basis sets[4]. Finally, comparing levels 1 and 4 allows us to see the difference of employing DFT-based method versus wavefunction-based method, domain-based local pair natural orbital–coupled cluster with perturbative triple excitations (DLPNO-CCSD(T)) calculations[7,8] for single point energy correction.

The pathway for the 4-membered, stepwise mechanism (*vide infra*) was initially used for benchmarking the potential energy surface (PES), Supplementary Figure 1. Within each level of theory, the Gibbs free energy for each species is taken relative to the sum of the Gibbs free energies of the reactants (MAA and PNA) (Supplementary Figure 1). We can see that the Gibbs free energies are quite similar (within 2–4 kcal mol^{-1}) whether we use the optimised geometries in the gas phase (level of theory 1) or the solvent phase (level of theory 2).
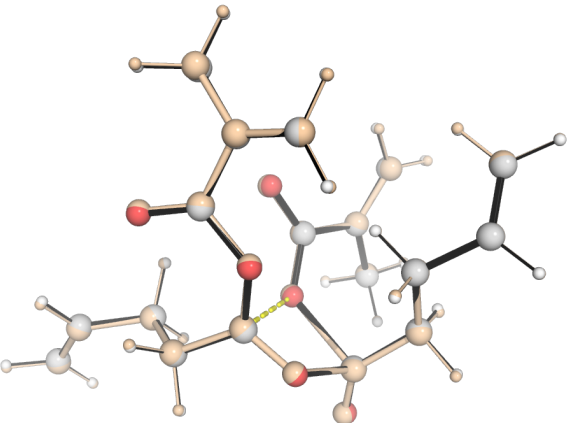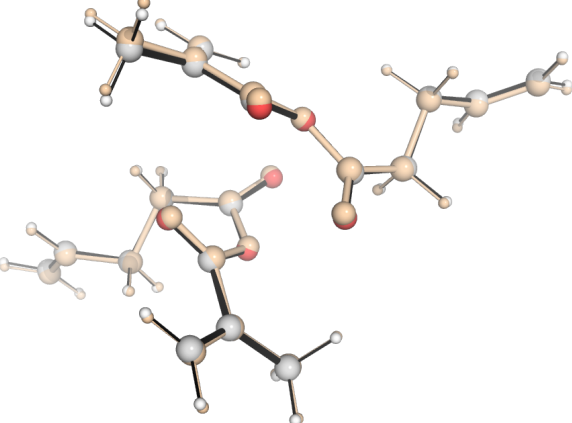
Further alignment of the DFT structures optimised in the gas phase and the solvent phase gives root mean square deviation (RMSD) values between 0.017Å and 0.207Å (Supplementary Figure 2). The RMSD values between structures under alignment were obtained by applying the `align` function in PyMOL software, which first uses a global dynamic-programming (Needleman–Wunsch[23]) alignment with BLOSUM62 scoring[24] to match atoms between the two structures. All atoms are superimposed by applying a least-squares fitting using the Kabsch algorithm[25] to minimize RMSD value. After this initial alignment, PyMOL performs up to five cycles of iterative refinement, discarding atoms with large deviations (typically beyond ~2 Å or two standard deviations) and repeating the fit until convergence. The final RMSD value after these procedures is then reported. The structures with larger RMSD values (**INT2-4m** at 0.207Å and **TS2a-4m** at 0.200Å) have Gibbs free energy values differing > 2 kcal mol^{-1} (but < 4 kcal mol^{-1}) whereas the structures with small RMSD values have very similar Gibbs free energy values (within 2 kcal mol^{-1}). Overall, the Gibbs free energies between these two methods are similar.
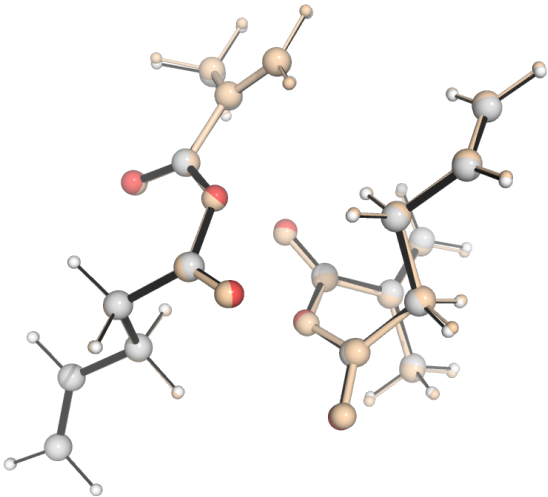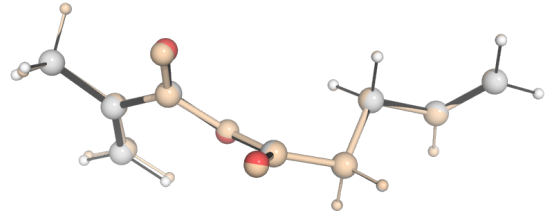
Comparing levels of theory 1 and 3, the use of Pople basis sets with diffuse functions gives ~ 2–3 kcal mol^{-1} lower values for each species. Comparing the single point correction using SMD(CHCl$_3$)-M06-2X/def2-TZVP//M06-2X/def2-SVP (level of theory 1) and SMD(CHCl$_3$)-DLPNO-CCSD(T)/CBS//M06-2X/def2-SVP (level of theory 4), we see that the intermediates/minima on the PES have almost the same Gibbs free energies, while the TSs for these two theories are within 2 kcal mol^{-1} (no systematic trend). Overall, the choice of either method would be equally valid for the study of the present system. As the Karlsruhe-family basis sets can provide a more well-balanced description for all elements across the periodic table, and the DLPNO-CCSD(T)/CBS is generally considered to be close to the "gold standard" of quantum chemistry CCSD(T)/CBS,[26,27] we applied level of theory 4, SMD(CHCl$_3$)-DLPNO-CCSD(T)/CBS//M06-2X/def2-SVP, for all subsequent studies.
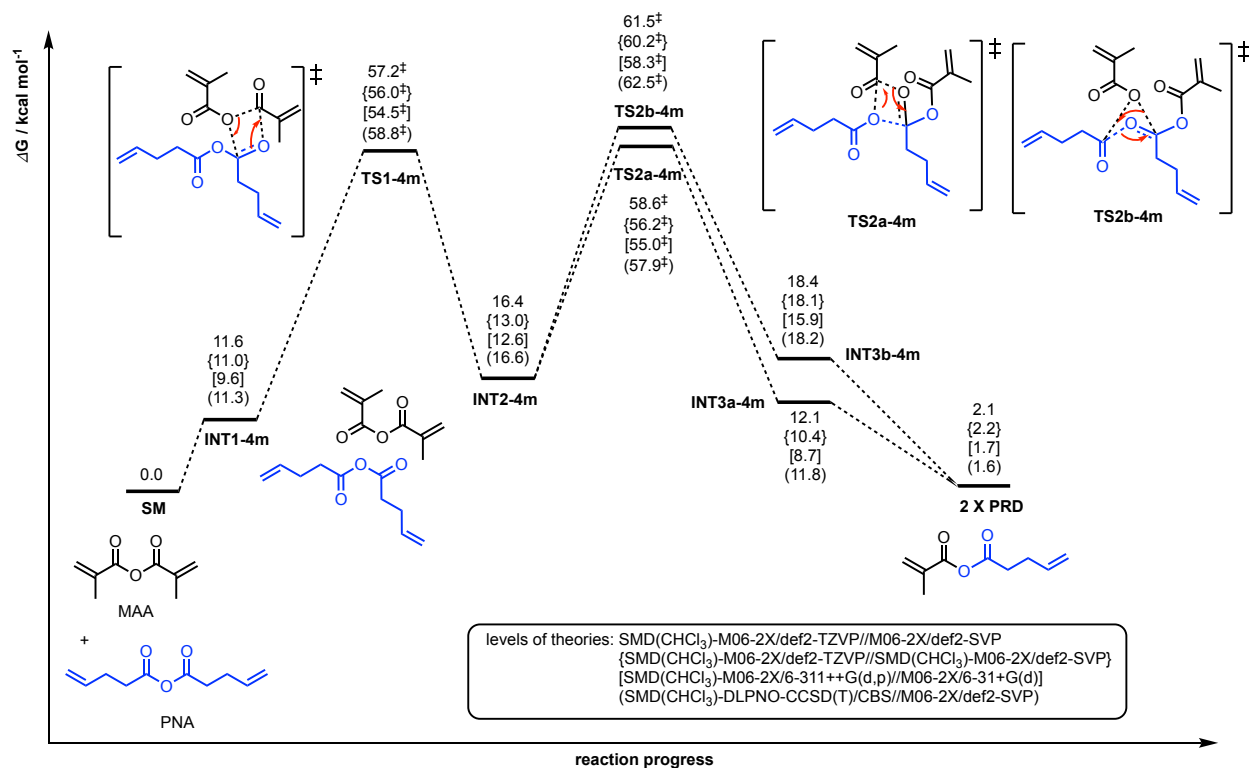
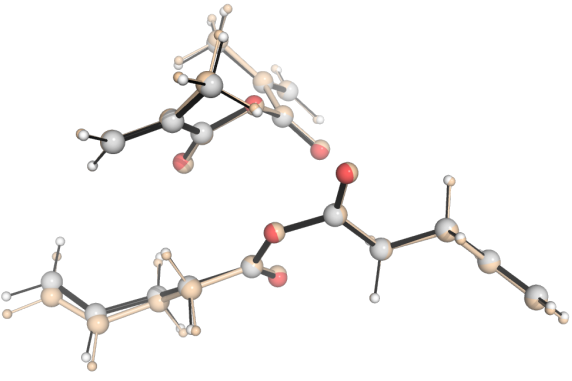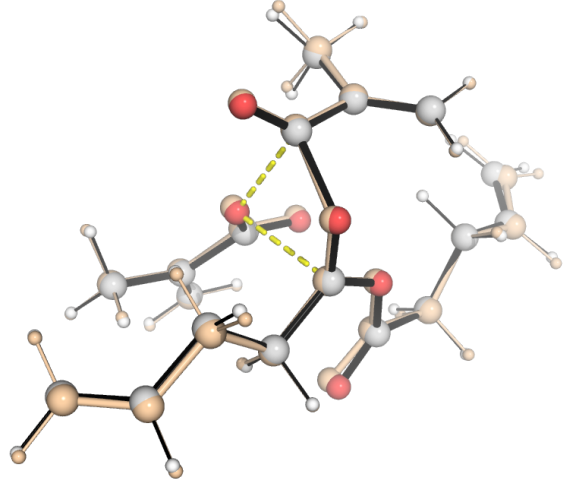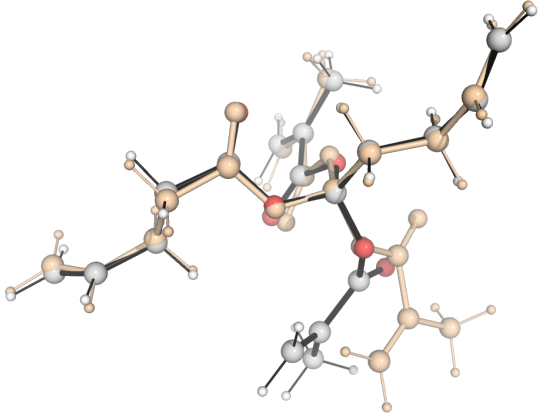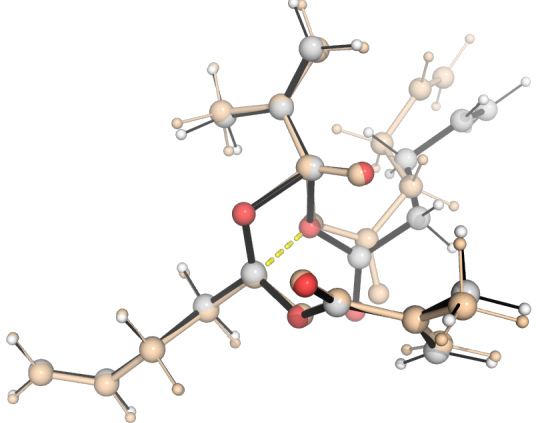**Supplementary Figure 1.** Gibbs free energy profile for the dynamic covalent bond exchange via 4-membered transition states (TSs). Four different levels of theories were considered and the values are given for 1) SMD(CHCl$_3$)-M06-2X/def2-TZVP//M06-2X/def2-SVP and 2) SMD(CHCl$_3$)-M06-2X/def2-TZVP//SMD(CHCl$_3$)-M06-2X/def2-SVP in curly braces and 3) SMD(CHCl$_3$)-M06-2X/6-311++G(d,p)//M06-2X/6-31+G(d) in square brackets, and 4) SMD(CHCl$_3$)-DLPNO-CCSD(T)/CBS//M06-2X/def2-SVP in round brackets. CBS = complete basis set, which results from the extrapolation using double-/triple-ζ cc-pV(DT)Z basis sets.

PNA	MAA
RMSD = 0.020 Å	0.017 Å
INT1-4m	**TS1-4m**
RMSD = 0.073 Å	0.098 Å

S5
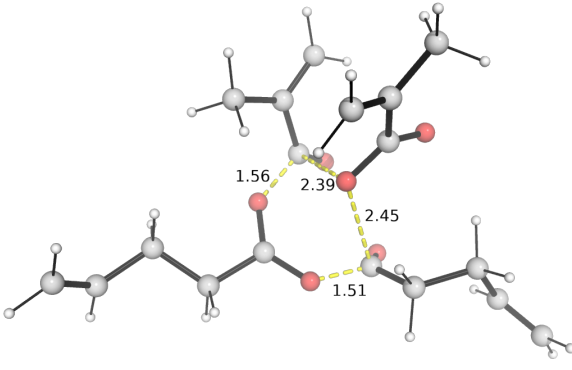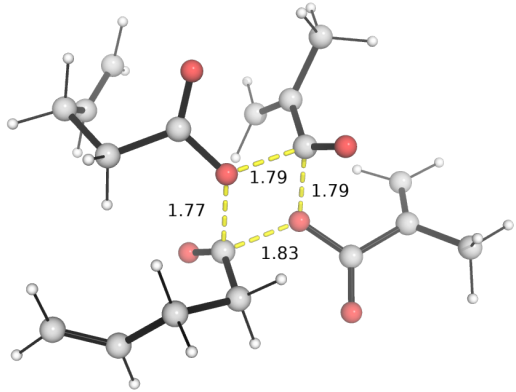
INT2-4m	**TS2a-4m**
RMSD = 0.207 Å	0.200 Å
TS2b-4m	**INT3a-4m**
RMSD = 0.041 Å	0.081 Å

INT3b-4m	PRD
RMSD = 0.064 Å	0.019 Å

Supplementary Figure 2. Overlay of DFT-optimised structures in gas phase (M06-2X/def2-SVP, normal color) and in solvent phase (SMD(CHCl$_3$)-M06-2X/def2-SVP, colored in pale orange) with RMSE value given in Å.

II.2 Concerted mechanism

Firstly, the concerted mechanism was considered (Scheme 2i, pathway a in the main text). An initial "opt=modredundant" constrained TS search with Gaussian gives a good guess structure with desired vibrations, however, upon removing the constraints for a full TS search, no TS structure was located. In addition, the Gaussian *"opt=QST2"* method was applied for the TS search and no positive result was obtained. The ORCA NEB-TS algorithm was used to locate the TS for the concerted mechanism; however, no TS was found.

TS_concerted_6m	TS_concerted_4m
$\Delta G^{\ddagger}$ = 59.3 kcal mol^{-1}	$\Delta G^{\ddagger}$ = 59.3 kcal mol^{-1}

Supplementary Figure 3. DFT optimised structures with key bond distances given in Å.

Upon several trials using the Gaussian *"opt=QST3"* method, we successfully located the TS for the concerted mechanism via 6-membered ring (**TS_concerted_6m**, Supplementary Figure 3). This TS is verified to connect to the desired sides of the reaction by performing IRC analysis (IRC movie in folder *DFT_structures_and_IRC_movie*). Upon solvation correction, this TS gives an activation barrier of 59.3 kcal mol^{-1}. This barrier is much higher than the ones computed for the stepwise mechanism (*vide infra*). An attempt on the conformational sampling of this TS using CREST program was unsuccessful (CREST conformers from this conformational sampling, when used for DFT TS search, did not yield any positive result). We additionally located the concerted mechanism via 4-membered ring (**TS_concerted_4m**, Supplementary Figure 3), which also has a very high barrier, at 59.3 kcal mol^{-1} (IRC movie also attached in folder *DFT_structures_and_IRC_movie*). Therefore, a concerted mechanism for the anhydride bond exchange is ruled out. This high barrier may be due to that the carbonyl group is not activated by, e.g., a Lewis acid or acid coordination to increase its nucleophilicity at carbonyl carbon for nucleophilic attack.

II.3 Relaxed potential energy surface (PES) scan

We considered a relaxed PES scan along the anhydride oxygen atom of MAA and the carbonyl carbon atom of PNA. The scan result is shown in Supplementary Figure 4. As we can see, as the anhydride oxygen atom approaches the carbonyl carbon (shortening O–C distances from structure 1 to structure 2 then to structure 3), the relative energy increases to ~ 60 kcal mol^{-1}. This indicates that there is a large barrier for the formation of O–C bond between the anhydride oxygen atom of MAA and the carbonyl carbon atom of PNA, requiring surmounting a barrier of at least 60 kcal mol^{-1}.
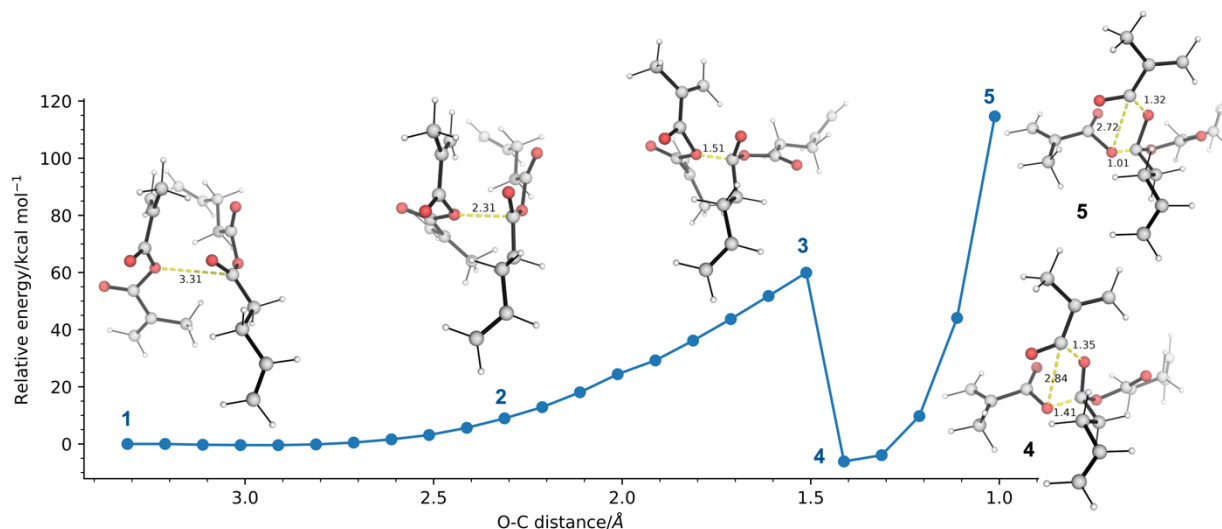
Supplementary Figure 4. Relaxed PES scan energy profile along the O-C distance using M06-2X/def2-SVP level of theory in the gas phase. Gas-phase energy values are used without further corrections.

This barrier will be unfavourable at the reaction conditions. We note that upon going from structure 3 to structure 4 (bond distance shortens from 1.51 Å to 1.41 Å, Supplementary Figure 4), the C–

O bond in the anhydride group of MAA breaks (bond distance of 2.84 Å in structure 4), while the carbonyl carbon forms new C–O bond with the carbonyl oxygen of PNA (bond distance of 1.35 Å in structure 4). This structure (structure 4) is thermodynamically downhill/more stable compared to the reactant complex (structure 1). As the bond distance further shortens to 1.01 Å (structure 5), the energy raises to > 100 kcal mol^{-1}, as the O–C bond is shortened beyond the equilibrium O–C bonding distance.

II.4 Alternative mechanisms

In Supplementary Figure 1, the methacrylic anhydride (MAA) C–O σ-bond is broken in the 4-membered TS structure, **TS1-4m**. We considered the second possibility where the 4-pentenoic anhydride (PNA) σ-bond is broken in a 4-membered TS structure (**TS1'-4m**) and the Gibbs free energy profile is shown in Supplementary Figure 5.
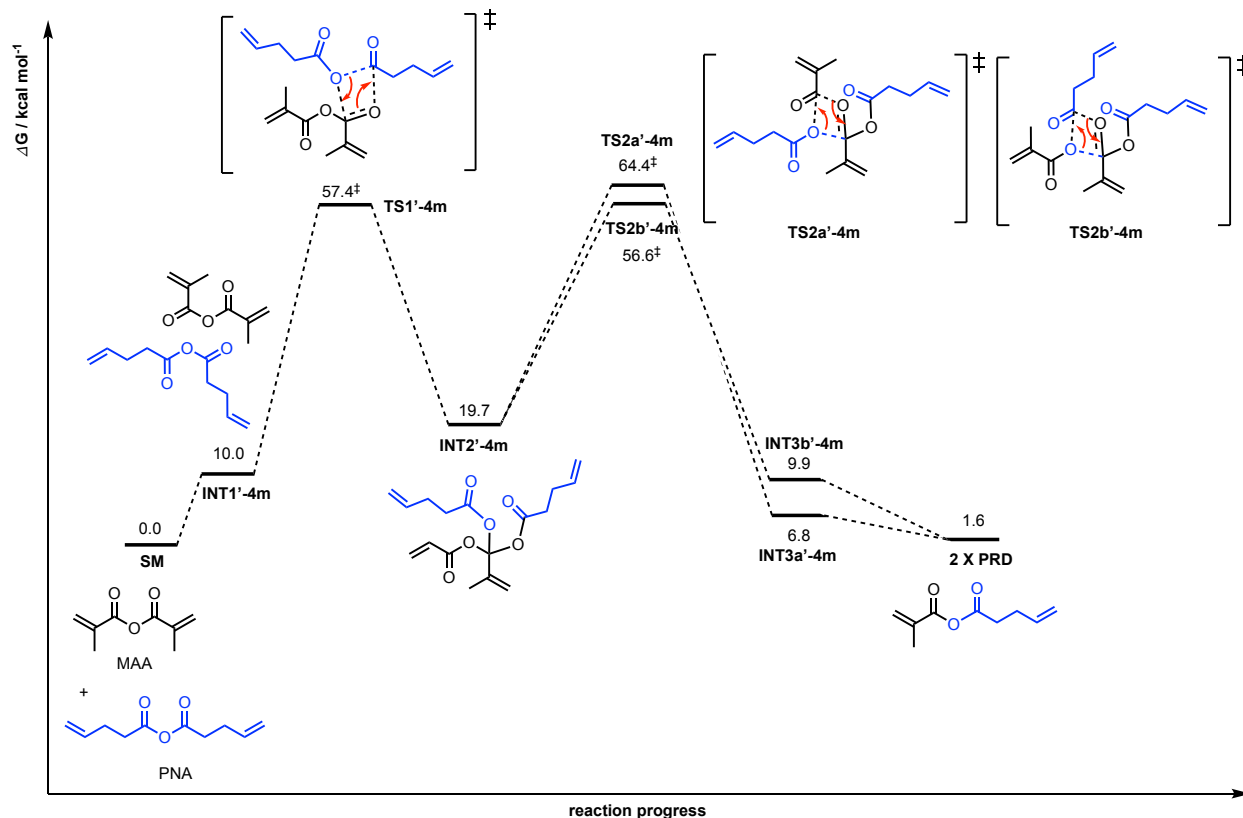
Supplementary Figure 5. Gibbs free energy profile for the dynamic covalent bond exchange via 4-membered TSs, computed at the SMD(CHCl$_3$)-DLPNO-CCSD(T)/CBS//M06-2X/def2-SVP level of theory. CBS = complete basis set, which results from the extrapolation using double-/triple-ζ cc-pV(DT)Z basis sets.

The Gibbs free energy profile via the 6-membered TS is shown in Supplementary Figure 6. The activation barrier of the first step was found to be slightly higher than that of the second step. This 6-membered TS, **TS1-6m** has a much lower barrier, at 50.1 kcal mol^{-1}, than **TS1-4m**. The barrier difference of 7.8 kcal mol^{-1} suggests that **TS1-6m** will be kinetically favoured over **TS1-4m** by a factor of > 522,000 : 1, using simple transition state theory (TST) as an estimate at 25ºC.
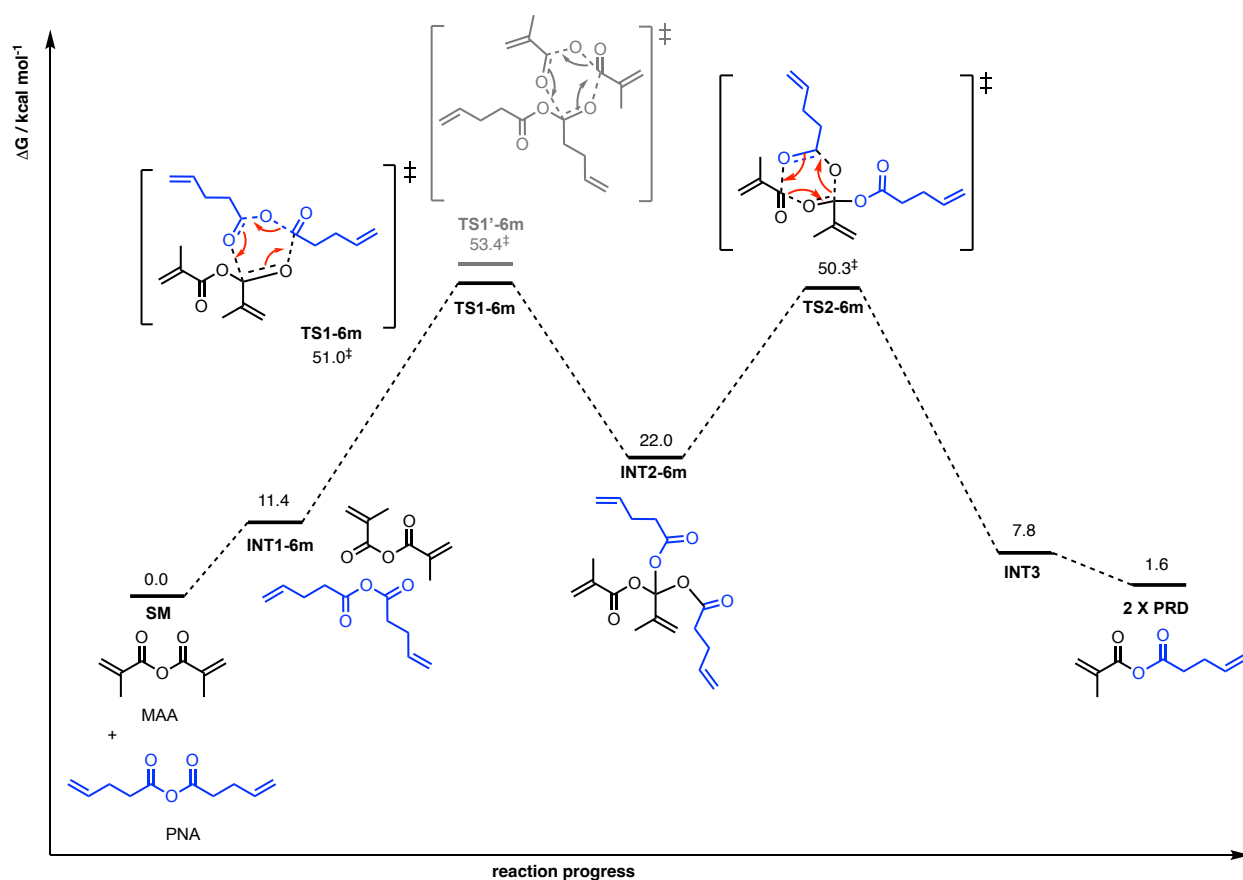
Supplementary Figure 6. Gibbs free energy profile for the dynamic covalent bond exchange via 6-membered TSs, computed at the SMD(CHCl₃)-DLPNO-CCSD(T)/CBS//M06-2X/def2-SVP level of theory. CBS = complete basis set, which results from the extrapolation using double-/triple-ζ cc-pV(DT)Z basis sets.

II.5 Conformational sampling

We performed thorough conformational sampling to determine each step of the reaction pathway. We do so for the reaction pathways occurring via 6-membered TSs and ignore the pathways via 4-membered TSs, the latter of which are expected to have higher and less favourable activation barrier than the former (compare Supplementary Figures 5 and 6).

II.6 Bond dissociation enthalpies (BDEs)

The bond dissociation enthalpies (BDEs) of the two different anhydride substrates, methacrylic anhydride (MAA) and 4-pentenoic anhydride (PNA) were computed in the gas phase at M06-2X/def2-SVP level of theory. The corresponding radicals were optimised, using unrestricted KS-DFT formalism. The BDE is calculated as

$$\mathrm{BDE(RCOO-COR)} = H_{\mathrm{RCOO\cdot}} + H_{\mathrm{RCO\cdot}} - H_{\mathrm{RCOO-COR}}$$

The BDE values for C–O bond in MAA and PNA are very similar, at 99.8 kcal mol⁻¹ for MAA and 99.3 kcal mol⁻¹ for PNA.

A potential radical mechanism was considered, by locating the TSs for the diradical formation via the breaking of C–O bond in MAA and PNA. These barriers are found to be 83.3 kcal/mol for MAA and 86.2 kcal/mol for PNA. Thus, potential mechanism via diradical species was ruled out.

II.7 Correlation with experimental data

The kinetics for the anhydride bond exchange using MAA and PNA small molecules as model system have been measured experimentally using ^{13}C NMR spectroscopy in CDCl$_3$ in a heated sealed tube.[22] The relevant kinetic data are shown below:

T/ºC	T/K	k	1/T	ln(k)	ln(k/T)
35	308.15	6.92E-07	0.00324517	-14.184	-19.914
40	313.15	1.42E-06	0.00319336	-13.465	-19.212
45	318.15	2.89E-06	0.00314317	-12.754	-18.517
50	323.15	1.77E-05	0.00309454	-10.942	-16.720

Supplementary Table 1. Kinetic parameters measured experimentally using ^{13}C NMR for the anhydride bond exchange between methacrylic anhydride (MAA) and 4-pentenoic anhydride (PNA).

We plot the Arrhenius plot of ln(k) against 1/T to obtain the following graph:

$$y = -20711.80x + 52.80$$
$$R^2: 0.93$$
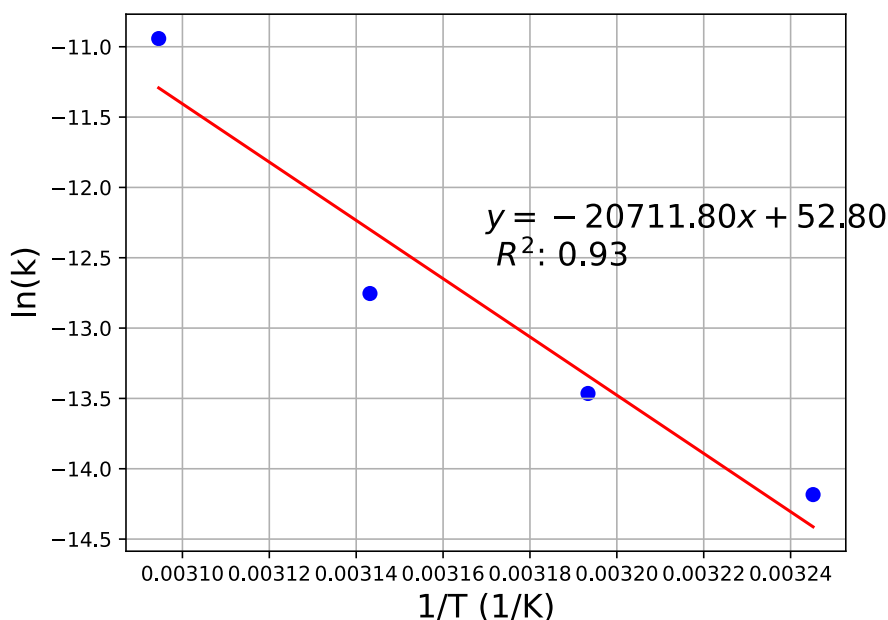
Supplementary Figure 7. Arrhenius plot for the anhydride bond exchange between methacrylic anhydride (MAA) and 4-pentenoic anhydride (PNA).

We can obtain the activation energy from the plot via:

$$\text{y-intercept} = \frac{-E_a}{R} = -20711.80$$
$$\implies E_a = 20711.80 * 8.314 = 41.2 kcal/mol$$

Thus, the enthalpy of activation is given by

$$E_a = \Delta H^\ddagger + RT$$
$$\implies \Delta H^\ddagger = E_a - RT = 41.2 - 8.314 * 323.15/4184$$
$$= 40.5 \text{ kcal/mol}$$

Using the Eyring-Polanyi plot of $\ln(k/T)$ against $1/T$ (Supplementary Figure 8), we obtain the following the entropy of activation as:

$$\text{y-intercept} = \frac{\Delta S^\ddagger}{R} + ln\frac{k_B}{h} = 46.05$$
$$\frac{\Delta S^\ddagger}{8.314} + ln\frac{1.380649E^{-23}}{6.62607015E^{-34}} = 46.05$$
$$\frac{\Delta S^\ddagger}{8.314} = 46.05 - 23.76 = 22.29$$
$$\Delta S^\ddagger = 22.29 * 8.314/4184 = 0.04429 \text{ kcal/mol/K}$$
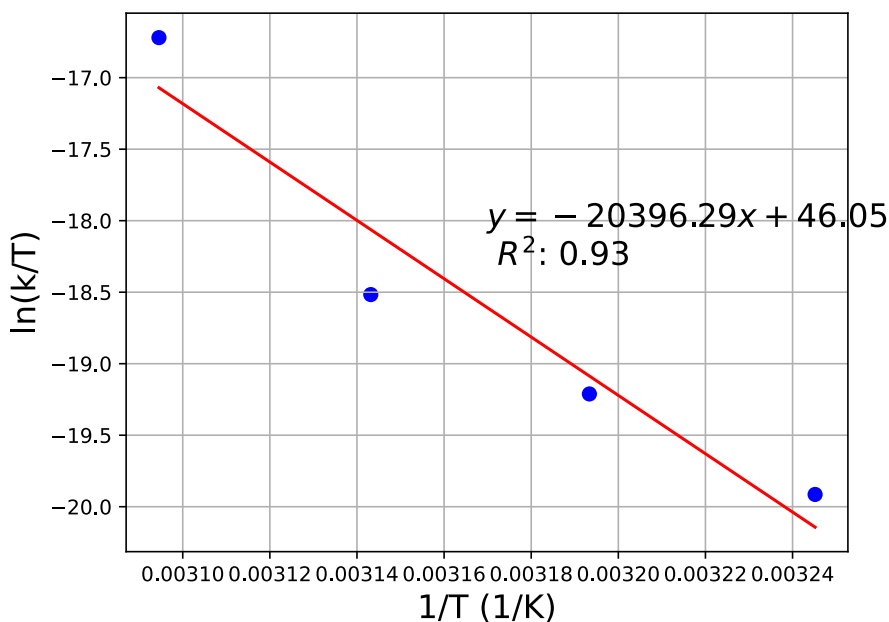
Supplementary Figure 8. Eyring-Polanyi plot for the anhydride bond exchange between methacrylic anhydride (MAA) and 4-pentenoic anhydride (PNA).

Therefore, we can obtain the experimental Gibbs free energy of activation as:

$$\Delta G^\ddagger = \Delta H^\ddagger - T * \Delta S^\ddagger$$
$$= 40.5 - 323.15 * 0.04429$$
$$= 26.2 \text{ kcal/mol}$$

We applied the same method to convert the enthalpy of activation for acid-anhydride bond exchange reported by the Chen group[28] (Supplementary Table 2) into Gibbs free energy.

T/°C	T/K	k	1/T	ln(k)	ln(k/T)
180	453.15	0.000233	0.002207	-8.36544	-14.4817
185	458.15	0.000355	0.002183	-7.94307	-14.0703
195	468.15	0.001093	0.002136	-6.81892	-12.9677
200	473.15	0.002227	0.002113	-6.10702	-12.2664

Supplementary Table 2. Kinetic parameters measured experimentally for the acid-anhydride bond exchange reported by the Chen group.
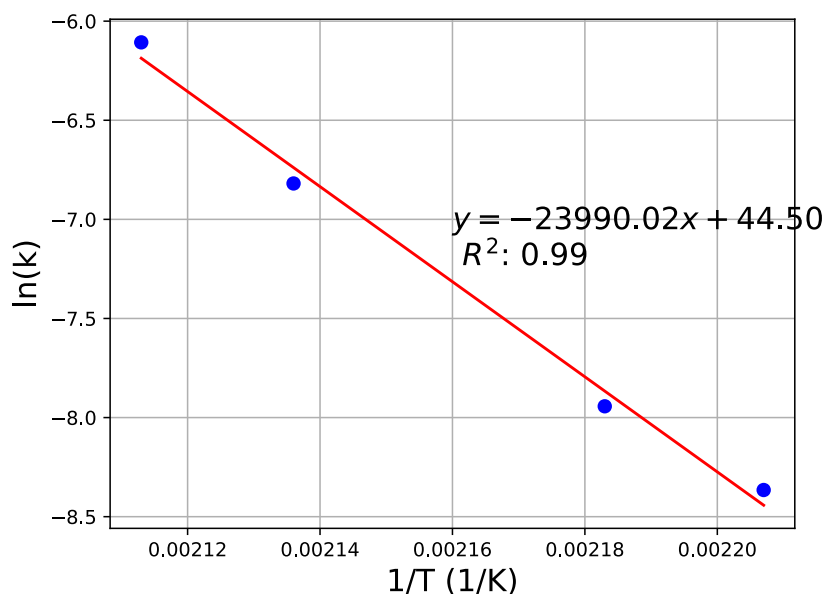
Supplementary Figure 9. Arrhenius plot for the anhydride bond exchange in tri-block copolymer.

We can obtain the activation energy from this plot (Supplementary Figure 9):

$$\text{y-intercept} = \frac{-E_a}{R} = -23990.02$$

$$\implies E_a = 23990.02 * 8.314 = 47.7\text{kcal/mol}$$

Thus, the enthalpy of activation is given by

$$E_a = \Delta H^{\ddagger} + RT$$

$$\implies \Delta H^{\ddagger} = E_a - RT = 47.7 - 8.314 * 323.15/4184$$

$$= 47.1\text{kcal/mol}$$

Using the Eyring-Polanyi plot of ln(k/T) against 1/T (Supplementary Figure 10), we obtain the following the entropy of activation as:

$$\text{y-intercept} = \frac{\Delta S^{\ddagger}}{R} + \ln\frac{k_B}{h} = 35.39$$

$$\frac{\Delta S^{\ddagger}}{8.314} + \ln\frac{1.380649E^{-23}}{6.62607015E^{-34}} = 35.39$$

$$\frac{\Delta S^{\ddagger}}{8.314} = 35.39 - 23.76 = 11.63$$

$$\Delta S^{\ddagger} = 11.63 * 8.314/4184 = 0.02310989961 \text{kcal/mol/K}$$

Eyring-Polanyi plot. Axis labels: $\ln(k/T)$ vs $1/T$ (1/K). Fit line: $y = -15410.72x + 35.39$, R^2: 0.97
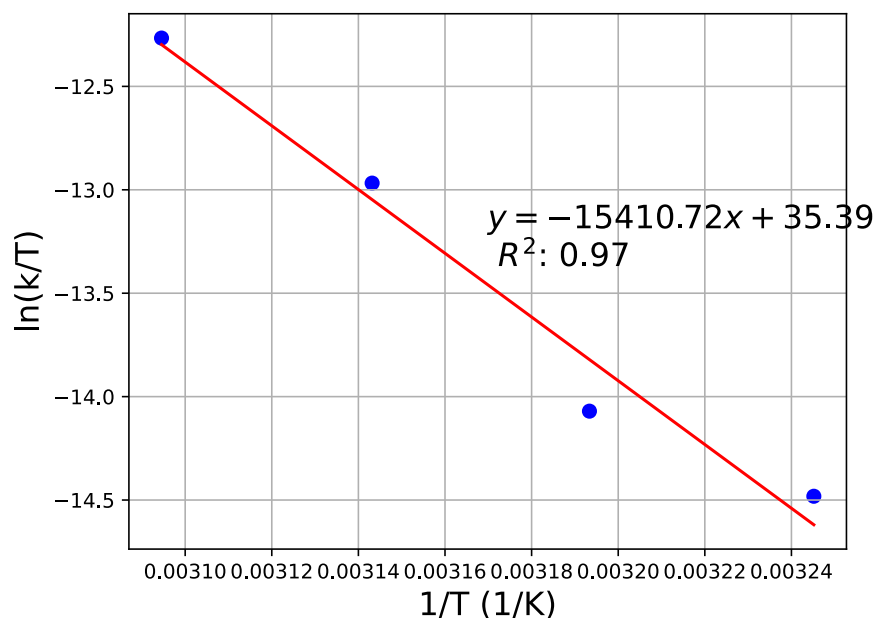
Supplementary Figure 10. Eyring-Polanyi plot for the anhydride bond exchange in tri-block copolymer.

Therefore, we can obtain the experimental Gibbs free energy of activation, at 200°C, as:
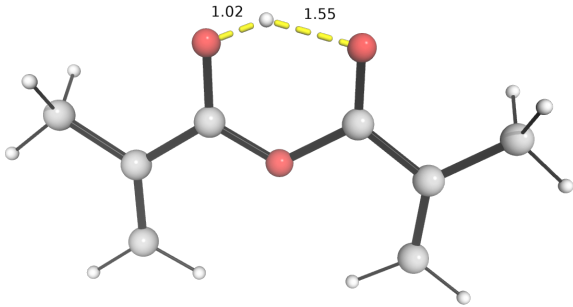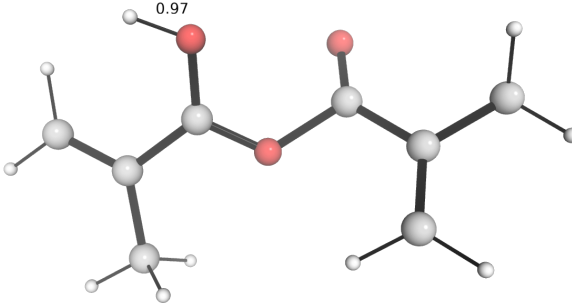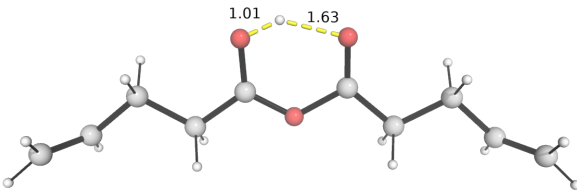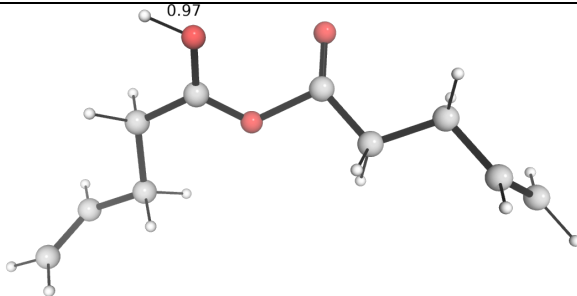
$$\Delta G^{\ddagger} = \Delta H^{\ddagger} - T * \Delta S^{\ddagger}$$
$$= 47.1 - 473.15 * 0.0231099$$
$$= 36.2 \text{kcal/mol}$$

II.8 Mechanism under acid catalysis

After considering all the mechanistic possibilities, we note that the barriers in the absence of acid catalysis are rather high. The acid-catalysed anhydride exchange mechanism has been studied experimentally by Mironov and Zharkov, whose earlier works showed that anhydride bond exchange can occur readily under acid-catalysis conditions.[22] We performed computational studies to explore this possibility.

We follow the approach for studying the site of protonation by adding a naked proton, as reported by Grimme's work.[29] Since our system has two distinct possible sites for protonation, namely the anhydride carbonyl O atom and the bridging O atom, we investigated the relative stabilities of the

protonated species for each possibility for both MAA and PNA monomer. For both monomers, the starting structure where the proton is near the bridging O atom optimises to the structure where the proton is on one carbonyl O atom (**[MAA-H+]_O2** and **[PNA-H+]_O2**). The optimised DFT structures and their relative Gibbs free energies are given in Supplementary Figure 11.

[MAA-H+]_O1	[MAA-H+]_O2
$\Delta\Delta G^{\ddagger} = 0.0$ kcal mol^{-1}	$\Delta\Delta G^{\ddagger} = 3.8$ kcal mol^{-1}
[PNA-H+]_O1	[PNA-H+]_O2
$\Delta\Delta G^{\ddagger} = 1.4$ kcal mol^{-1}	$\Delta\Delta G^{\ddagger} = 3.6$ kcal mol^{-1}

Supplementary Figure 11. DFT optimised structures for the PNA and MAA monomer, with their Gibbs free energies for the protonation process given relative to the most stable structure, **[MAA-H+]_O1**, which forms the proton-bridged 6-member ring.

The TS structure for the cycloaddition via 8-member ring transition state was verified to be the true transition state leading from the reactant complex to the intermediate via IRC analysis (see IRC movie attached). Without conformational sampling, this TS, **TS_acid'**, has a barrier of 30.0 kcal/mol, which upon further conformational sampling and DFT TS optimization, reduced to 25.9 kcal/mol, **TS_acid**, in Supplementary Figure 12.

TS_acid	TS_acid'
$\Delta G^{\ddagger} = 25.9$ kcal mol^{-1}	$\Delta G^{\ddagger} = 30.0$ kcal mol^{-1}
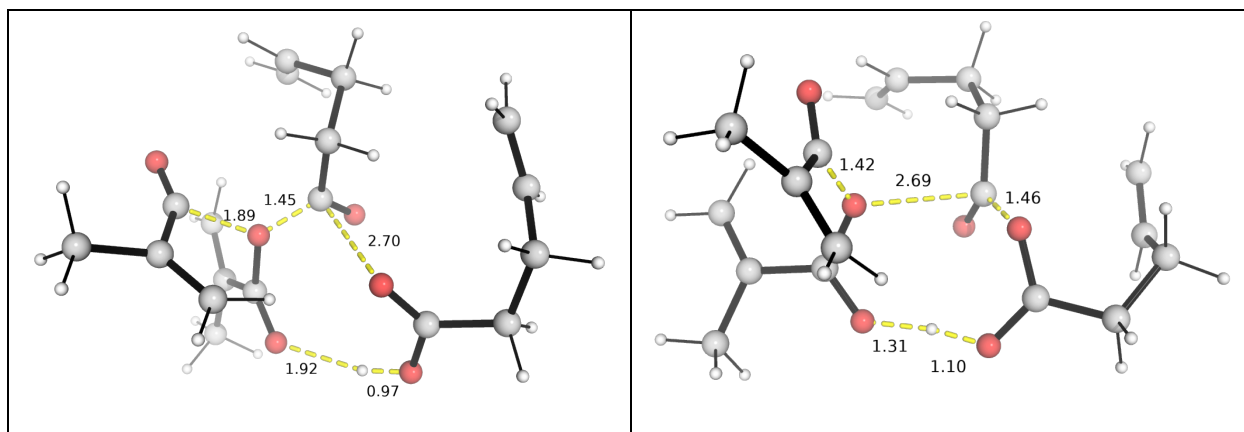
Supplementary Figure 12. DFT optimised structures for anhydride bond exchange under acid calaysis, with key bond distances given in Å. Gibbs free energies are given with respect to the reactant complex, **RCT_acid**.

II.9 Effect of Temperature on Gibbs free energy correction

The Gibbs free energy profile has been computed with temperature correction at 25ºC to check against the experimentally obtained barrier using 13C NMR spectroscopy in CDCl3.[22] To assess the effect of temperature change on the activation barriers and the Gibbs free energy profile, we recomputed Gibbs free energy profile for the uncatalysed and acid-catalysed reaction in different temperatures (50ºC, 100ºC, 150ºC, 180ºC, 200ºC). The results are summarised in Tables S3–5 below.

We see that for uncatalysed system, the dynamic covalent bond exchange mechanism via 6-membered ring transition states involving the breaking of C–O bond in **MAA** (Supplementary Table 3) is still favoured over breaking of C–O bond in **PNA** (Supplementary Table 4), at all temperatures, such that the preferred pathway will proceed via Scheme 3a, main text. The overall barrier ranges from 44.1 kcal/mol at 25ºC, to 52.8 kcal/mol at 200ºC for uncatalysed reaction, although the barrier from **INT1** to **TS1** stay in the range of 35.1 kcal/mol at 25ºC to 36.1 kcal/mol at 200ºC (Supplementary Table 3). The increase in the barrier can be rationalised as such: as temperature increases, the molecules will move with a higher kinetic energy, making the formation of (reactant and TS) complex more difficult. Further analysis using the energies of (**TS1** – **MAA** – **PNA**) shows that in this process, the $\Delta H^{\ddagger}$ component of $\Delta G^{\ddagger} = \Delta H^{\ddagger} - T\Delta S^{\ddagger}$ remains similar across different temperatures (28.4 kcal/mol at 25ºC to 28.6 kcal/mol at 200ºC) whereas the $-T\Delta S^{\ddagger}$ term increases from 15.3 kcal/mol at 25ºC to 23.7 kcal/mol at 200ºC, without quasi-RRHO correction and from 15.6 kcal/mol at 25ºC to 24.2 kcal/mol at 200ºC, with quasi-RRHO correction. Thus, the temperature increase mostly affects the term $-T\Delta S^{\ddagger}$, due to its temperature contribution.

For the acid catalysed reaction, a similar trend is observed: the barrier increases from 25.6 kcal/mol at 25ºC to 33.2 kcal/mol at 200ºC (Supplementary Table 5), although the barriers from **INT1_acid** to **TS1_acid** remain in a narrow range (24.1 kcal/mol at 25ºC to 24.2 kcal/mol at 200ºC, Supplementary Table 5).

T/°C	INT1	TS1	INT2	TS2a	TS2b	INT3	PRD	TS1 – INT1
25	9.0	**44.1**	9.9	42.4	44.3	7.8	0.7	35.1
50	10.1	**45.3**	11.1	43.7	44.2	8.9	0.8	35.2
100	12.4	**47.8**	13.4	46.2	46.8	11.0	0.9	35.4
150	14.6	**50.3**	16.0	48.8	49.4	13.1	1.1	35.7
180	15.9	**51.8**	17.5	50.3	50.9	14.3	1.1	35.9
200	16.7	**52.8**	18.5	51.3	52.0	15.2	1.2	36.1

Supplementary Table 3. Gibbs free energies for species in the dynamic covalent bond exchange mechanism via 6-membered ring transition states involving the breaking of C–O bond in methacrylic anhydride (MAA), corresponding to Figure 2a in the main text. Values in bold indicate rate-determining step barrier.

T/°C	INT1	TS1'	INT2'	TS2a'	TS2b'	INT3	PRD	TS1'– INT1
25	9.0	**45.2**	12.3	44.2	46.2	7.8	0.7	36.2
50	10.1	**46.5**	13.5	45.5	47.4	8.9	0.8	36.4
100	12.4	**49.1**	16.0	48.0	49.9	11.0	0.9	36.7
150	14.6	**51.7**	18.5	50.5	52.3	13.1	1.1	37.1
180	15.9	**53.2**	19.9	52.0	53.8	14.3	1.1	37.3
200	16.7	**54.2**	20.9	53.0	54.8	15.2	1.2	37.5

Supplementary Table 4. Gibbs free energies for species in the dynamic covalent bond exchange mechanism via 6-membered ring transition states involving the breaking of C–O bond in 4-pentenoic anhydride (PNA), corresponding to Figure 2b in the main text. Values in bold indicate rate-determining step barrier.

T/°C	INT1_acid	TS1_acid	INT2_acid	PRD_acid	TS1_acid – INT1_acid
25	1.8	**25.9**	14.8	2.7	24.1
50	2.8	**26.9**	15.7	2.7	24.1
100	4.8	**29.0**	17.5	2.8	24.2
150	6.8	**30.1**	19.3	2.9	23.3

| 180 | 8.0 | **32.2** | 20.4 | 3.0 | 24.2 |
| 200 | 8.8 | **33.0** | 21.1 | 3.0 | 24.2 |

Supplementary Table 5. Gibbs free energies for species in the acid-catalysed dynamic covalent bond exchange mechanism. Values in bold indicate rate-determining step barrier.

II.10 Effect of inclusion of D3 correction in M06-2X in resulting Gibbs free energy profile

As suggested by one reviewer, we performed additional studies on the major pathway using M06-2X-D3/def2-SVP for geometry optimisation, followed by DLPNO-CCSD(T) single point solvent correction to ascertain the effect of inclusion of D3 correction on the Gibbs free energy profile. We took the lowest energy conformers of PES for the major pathway and performed additional studies by reoptimising the structures using M06-2X-D3, followed by SP DLPNO-CCSD(T) with solvent correction. The following show the comparison of energy profiles, with the SMD(chloroform)-DLPNO-CCSD(T)//M06-2X-D3/def2-SVP results in square brackets and originally computed SMD(chloroform)-DLPNO-CCSD(T)// M06-2X/def2- SVP shown. We observed that the energy profile thus obtained (Supplementary Figure 13) is no different either with D3 correction or not, when using M06-2X functional, in agreement with other studies.
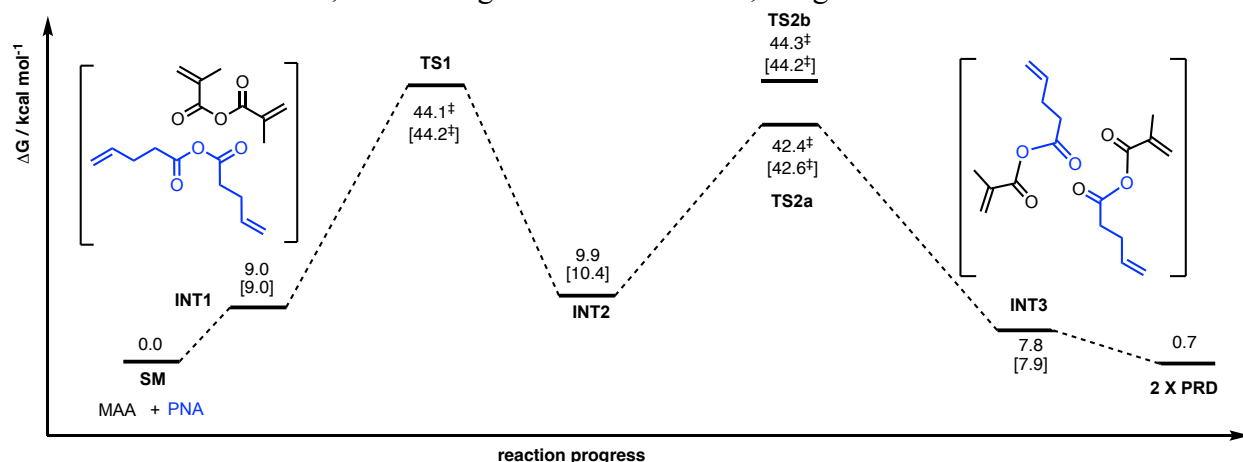
Supplementary Figure 13. Gibbs free energy profile for the dynamic covalent bond exchange via 6-membered TSs via Pathway I shown in Scheme 3a) in the main text. Shown are energies from SMD(chloroform)-DLPNO-CCSD(T)// M06-2X[-D3]/def2-SVP where the values in square brackets are results from the inclusion of D3 correction.

II.11 Effect of Boltzmann weighting in resulting Gibbs free energy profile

To access the effect of Boltzmann weighting on the potential energy surface, we performed Boltzmann weighting on the dynamic covalent bond exchange via 6-membered TSs via Pathway I shown in Scheme 3a) in the main text. The resulting comparison is shown in Supplementary Figure 14. We note a small change in the values for each species, but the overall conclusion that TS1 is the rate-determining step remains valid. For simplicity, we adopt the PES discussion without Boltzmann weighting but using the most stable conformer throughout, although we note

that, complete/adequate conformational sampling is required to ascertain the main rate-determining step.
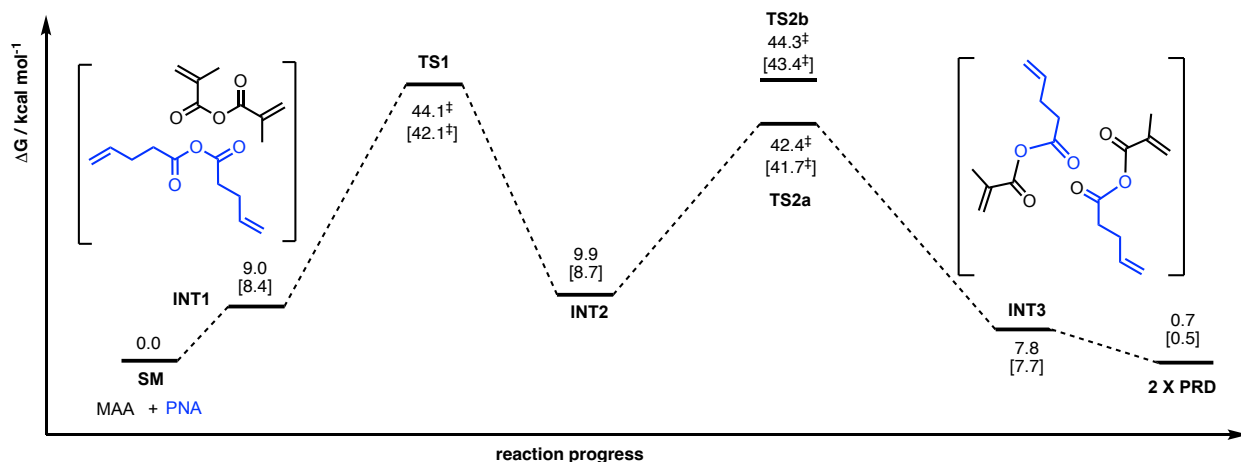
Supplementary Figure 14. Gibbs free energy profile for the dynamic covalent bond exchange via 6-membered TSs via Pathway I shown in Scheme 3a) in the main text. Shown are energies from SMD(chloroform)-DLPNO-CCSD(T)// M06-2X/def2-SVP where the values in square brackets are results from Boltzmann weighting.

II.12 Frontier molecular orbitals, natural bond orbital (NBO) charges, non-covalent interaction (NCI) plots and distortion-interaction/activation-strain analyses

To understand the molecular origins governing the transition state barrier heights, we performed frontier molecular orbitals (HOMO and LUMO plots), natural bond orbital (NBO) charges and distortion-interaction/activation-strain analyses for key transition states.

The NBO charges of the key atoms in the TSs, the HOMO and LUMO plots for the key TSs for both uncatalysed and catalysed pathways are shown in Supplementary Figure 15. The NBO charges analyses show that all the O atoms in the TSs for the uncatalysed pathways have similar charges at corresponding positions; these O atoms have NBO charges fall within a relative narrow range from -0.587 a.u. to -0.732 a.u.. In each TS for the uncatalysed pathways, the O atoms having the least negative and most negative NBO charges form part of the 6-membered ring in the TS structure (Supplementary Figure 15). For carbon atoms attached to the O atoms, corresponding carbon atoms in these TSs also have similar values – these are positively charged and with NBO charges in the range from 0.873 a.u. to 0.983 a.u.. These results indicate a concerted mechanism where the electrons flow from O to C, consistent with a nucleophilic attack on carbon. The consistent NBO charges among TSs indicate a similar electronic environment in all uncatalysed TS structures, suggesting that they proceed via similar mechanistic pathways.

For the catalysed pathway, transition state, **TS1_acid**, has O atom that has a much less negative NBO charge, such as one that is -0.369 a.u.. This is because this O atom is part of the fragment that forms the acylium ion (R–C≡O⁺), that has electrons donation to carbon atom (This species is subsequently attacked by a carboxylate to form the mixed anhydride). The greater charge distribution of the O atoms in the acid-catalysed pathway, as evidenced by larger differences in

charges (e.g., from -0.369 to -0.712 a.u.), also indicates a protonation-induced activation of the electrophilic site and better charge separation facilitated by the catalyst.

	NBO Charges	HOMO	LUMO
TS1			
TS2a			

TS2b			
TS1'			
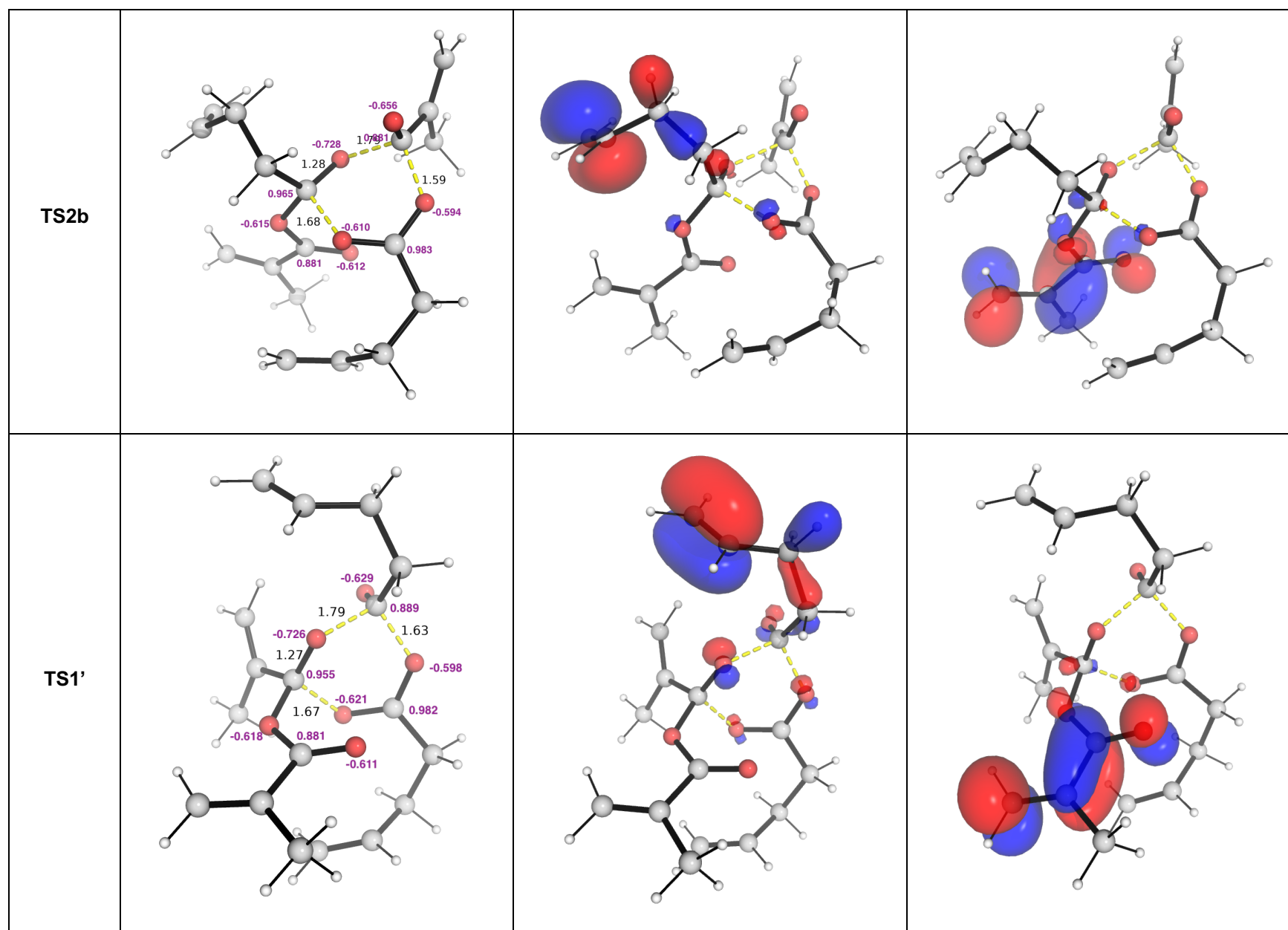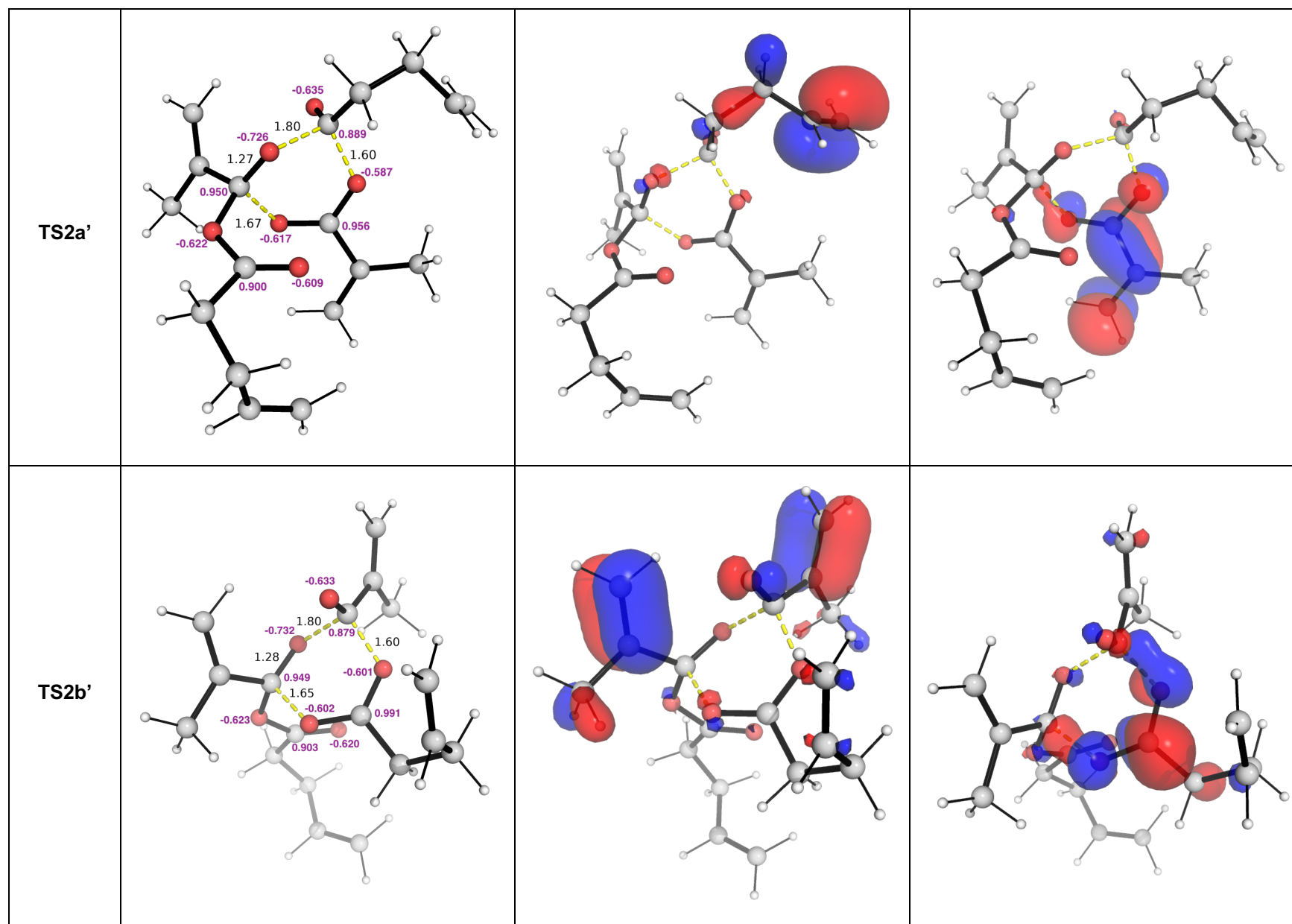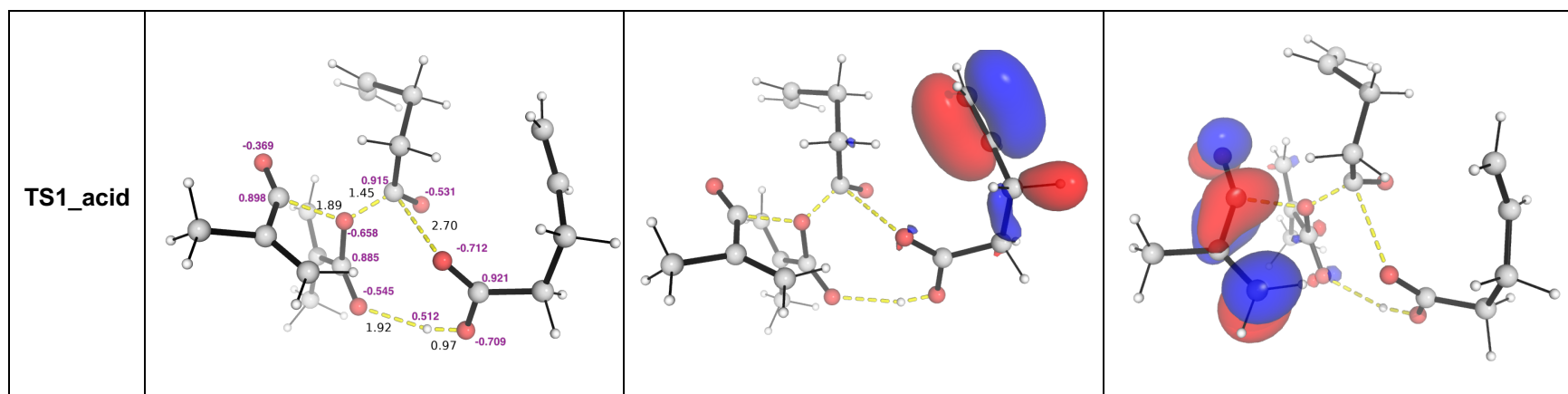
Supplementary Figure 15. Natural bonding orbital (NBO) charges for key atoms and frontier molecular orbital (FMO) plots including HOMO and LUMO plots for the lowest energy TSs for both uncatalysed and catalysed reaction pathways.

Analysis of the FMO plots indicates that the FMO structures are similar, with the notable exception in **TS2b'**. However, despite this noted difference, both the HOMO and LUMO have dominant coefficients on the peripheral of the reacting species and not form core of the 6-membered transition state ring (Supplementary Figure 15). Notably, the HOMO is largely localised on the electron-rich π bonds on C=C side group of the reacting monomers, which may suggest that nucleophilic attack or electron donation originates from regions outside the ring, thus helping to initiate and/or stabilise the TS. For the LUMO, it is mostly localised on the π^* systems of carboxylate group, implying that electrophilic activation occurs peripherally, and the 6-membered ring TS forms as a consequence of these interactions. These analysis may also suggest that the atoms within the 6-membered ring TS may be electronically neutral.

Distortion-interaction[30–32] analysis is applied to key TSs to discern the factors affecting the barriers of the lowest energy transition states in each mechanistic pathway. The transition state structures are decomposed by dividing the PNA and the MAA monomers as components. For the acid catalysed transition state, TS1_acid, the two components are the neutral PNA and the protonated MAA, since the protonation of MAA is more favoured than the protonation of PNA (Supplementary Figure 11). Single point calculations with SMD(chloroform) solvent correction were applied performed at DLPNO-CCSD(T)/CBS level of theory to obtain distortion and interaction energies. The distortion energy is given by:

$$E_{dist} = E_{TS,frag1} + E_{TS,frag2} - (E_{eq,frag1} + E_{eq,frag2})$$

where *TS,frag1,2* represent individual fragments in their distorted transition state geometries; and *eq,frag1,2* represent individual fragments in their optimized, equilibrium ground-state geometries; the interaction energy is given by:

$$E_{int} = E_{TS} - (E_{TS,frag1} + E_{TS,frag2})$$

which accounts for the stabilizing interactions (e.g., electrostatic, orbital, dispersion) between the distorted fragments in the TS.

Thus, the total activation energy is given by:
$$\Delta E^{\ddagger} = E_{dist} + E_{int.}$$

Note that this single point activation energy and the activation energy differences $\Delta\Delta E^{\ddagger}$ between the TSs (**Supplementary Table 6**) may be different from the Gibbs free energy differences $\Delta\Delta G^{\ddagger}$

that is computed fully (including vibrational frequencies analysis) at SMD(chloroform)-DLPNO-CCSD(T)/CBS//M06-2X/def2-SVP level of theory.

Transition State	$\Delta E^\ddagger$	E_{dist}	E_{int}
TS1	28.1	43.6	-15.5
TS2a	26.2	171.5	-145.3
TS2b	27.5	164.1	-136.6
TS1'	28.6	49.0	-20.4
TS2a'	28.1	158.1	-130.0
TS2b'	30.4	180.4	-150.0
TS1_acid	13.5	232.0	-218.5

Supplementary Table 6. Distortion-interaction analysis applied to key transition states.

We note that this decomposition of TSs by dividing the PNA and the MAA monomers as components may work well for **TS1** and **TS1'** but not necessarily for **TS2a**, **TS2b**, **TS2a'**, **TS2b'**, since the anhydride monomer may have already undergone substantial geometry changes upon reaching the second TS. Nevertheless, we note that overall, the first step is rate-determining and that the high activation barriers arises predominantly due to the strain energies experienced by the reacting components when they reorganise in the 6-membered ring transition states.

III. DFT-optimised structures and absolute energies

Geometries of all optimised structures (in *.xyz* format with their associated energy in Hartrees) are included in a separate folder named *DFT_structures_and_IRC_movie* with an associated readme.txt file. All these data have been deposited with this Supplementary Information and uploaded to https://zenodo.org/records/16625442 (DOI: 10.5281/zenodo.16625442).

Supplementary Table 7. Absolute values (in Hartrees) for SCF energy, zero-point vibrational energy (ZPE), enthalpy and quasi-harmonic Gibbs free energy (at 25°C/298.15 K) for optimised structures are given below. Single point corrections in SMD Chloroform for the reaction studies or in C-PCM environments (varying dielectric constants) are also included.

Mechanistic studies for MAA + PNA anhydride bond exchange in gas phase						
Structure	E/au	ZPE/au	H/au	T.S/au	qh-G/au	SP DLPNO-CCSD(T)/ CBS
MAA_c1	-535.89586	0.167081	-535.71583	0.049232	-535.763003	-535.9324285

MAA_c2	-535.89439	0.167034	-535.71438	0.049479	-535.761613	-535.9321499
MAA_c3	-535.8936	0.167027	-535.71361	0.049549	-535.76081	-535.9314652
MAA_c4	-535.89458	0.167029	-535.71462	0.049292	-535.761752	-535.9309761
MAA_c5	-535.89458	0.16703	-535.71462	0.049291	-535.761751	-535.930976
MAA_c6	-535.89458	0.16703	-535.71462	0.049291	-535.761751	-535.930976
MAA_c7	-535.89458	0.167031	-535.71462	0.049289	-535.761749	-535.9309758
MAA_c8	-535.89458	0.167032	-535.71462	0.049287	-535.761747	-535.9309738
MAA_c9	-535.89345	0.167198	-535.7134	0.048927	-535.760242	-535.9298509
MAA_c10	-535.89345	0.167199	-535.7134	0.048923	-535.760239	-535.9298491
MAA_c11	-535.89347	0.166944	-535.7136	0.049391	-535.760744	-535.9292552
MAA_c12	-535.89296	0.167162	-535.71298	0.048819	-535.759725	-535.9292984
MAA_c13	-535.889	0.167235	-535.70906	0.047743	-535.755372	-535.9267171
MAA_c14	-535.8857	0.167331	-535.70577	0.047509	-535.751852	-535.9227985
PNA_c1	-614.40942	0.223918	-614.16965	0.058153	-614.22399	-614.4499867
PNA_c2	-614.41095	0.224743	-614.17089	0.055637	-614.22353	-614.4509797
PNA_c3	-614.41095	0.224743	-614.17089	0.055637	-614.22353	-614.4509794
PNA_c4	-614.41095	0.224743	-614.17089	0.055635	-614.223529	-614.4509789
PNA_c5	-614.41023	0.224985	-614.16997	0.055224	-614.222383	-614.4509257
PNA_c6	-614.41023	0.224985	-614.16997	0.055214	-614.22238	-614.4509218
PNA_c7	-614.41023	0.224986	-614.16997	0.055213	-614.222379	-614.4509217
PNA_c8	-614.41023	0.224986	-614.16998	0.055207	-614.222377	-614.4509226
PNA_c9	-614.41023	0.224988	-614.16997	0.05521	-614.222377	-614.4509207
PNA_c10	-614.41023	0.224988	-614.16997	0.055208	-614.222376	-614.4509194
PNA_c11	-614.41055	0.224572	-614.17055	0.056751	-614.223788	-614.4497136
PNA_c12	-614.41144	0.224793	-614.1714	0.055381	-614.22398	-614.4502281
PNA_c13	-614.41086	0.224617	-614.17094	0.055386	-614.223477	-614.4500614
PNA_c14	-614.41086	0.224621	-614.17093	0.055383	-614.223472	-614.4500605
PNA_c15	-614.41086	0.224621	-614.17093	0.055378	-614.22347	-614.4500609
PNA_c16	-614.41086	0.22462	-614.17093	0.055379	-614.223471	-614.4500584
PNA_c17	-614.41086	0.22462	-614.17093	0.05538	-614.223471	-614.4500581
PNA_c18	-614.41124	0.225072	-614.17089	0.056178	-614.223719	-614.4493537
PNA_c19	-614.41124	0.225073	-614.17089	0.056161	-614.223711	-614.4493525
PNA_c20	-614.40875	0.225214	-614.16822	0.056273	-614.221032	-614.449153

INT1	-1150.3323	0.393124	-1149.9106	0.086065	-1149.990279	-1150.391776
INT1_c2	-1150.333	0.393272	-1149.9111	0.086369	-1149.99099	-1150.391564
INT1_c3	-1150.3311	0.393767	-1149.9088	0.086285	-1149.988375	-1150.391147
INT1_c4	-1150.3331	0.393806	-1149.9109	0.085246	-1149.990118	-1150.390578
INT1_c5	-1150.3332	0.394064	-1149.9109	0.084557	-1149.989742	-1150.390786
INT1_c6	-1150.3303	0.393905	-1149.908	0.084474	-1149.987099	-1150.390368
INT1_c7	-1150.3326	0.393989	-1149.9103	0.085056	-1149.989449	-1150.390299
INT1_c8	-1150.3326	0.394017	-1149.9102	0.084957	-1149.989389	-1150.390294
INT1_c9	-1150.332	0.393853	-1149.9096	0.08537	-1149.989052	-1150.389639
INT1_c10	-1150.3325	0.393941	-1149.9102	0.085057	-1149.989462	-1150.38969
INT1_c11	-1150.3313	0.394082	-1149.9089	0.08612	-1149.98847	-1150.389265
INT1_c12	-1150.3308	0.393522	-1149.9087	0.085514	-1149.988149	-1150.388415
INT1_c13	-1150.3308	0.393535	-1149.9087	0.085473	-1149.988123	-1150.388403
INT1_c14	-1150.3312	0.393774	-1149.9091	0.085017	-1149.98821	-1150.388628
INT1_c15	-1150.3313	0.394046	-1149.909	0.084214	-1149.987712	-1150.389094
INT1_c16	-1150.3307	0.393762	-1149.9085	0.084657	-1149.987658	-1150.387931
INT1_c17	-1150.3307	0.393762	-1149.9085	0.084654	-1149.987655	-1150.387931
INT1_c18	-1150.3312	0.394157	-1149.9089	0.08371	-1149.987359	-1150.38805
INT1_c19	-1150.3297	0.393723	-1149.9077	0.08444	-1149.9866	-1150.386313
INT1_c20	-1150.3297	0.393716	-1149.9077	0.084466	-1149.986619	-1150.38627
TS1	-1150.2768	0.393127	-1149.8565	0.082945	-1149.933101	-1150.337611
TS1_c2	-1150.2767	0.393335	-1149.8564	0.081403	-1149.93218	-1150.337906
TS1_c3	-1150.2761	0.393071	-1149.8559	0.083192	-1149.932573	-1150.33664
TS1_c4	-1150.2761	0.393071	-1149.8559	0.083195	-1149.932574	-1150.336638
TS1_c5	-1150.2776	0.393484	-1149.8573	0.082244	-1149.933247	-1150.33726
TS1_c6	-1150.2777	0.393564	-1149.8573	0.08075	-1149.932754	-1150.337811
TS1_c7	-1150.2777	0.393566	-1149.8573	0.080745	-1149.932751	-1150.337811
TS1_c8	-1150.2783	0.393681	-1149.8578	0.080929	-1149.933344	-1150.337851
TS1_c9	-1150.279	0.393891	-1149.8585	0.080041	-1149.933523	-1150.33816
TS1_c10	-1150.2783	0.393635	-1149.8579	0.081453	-1149.933457	-1150.337438
TS1_c11	-1150.2783	0.393806	-1149.8578	0.080368	-1149.933072	-1150.337876
TS1_c12	-1150.2744	0.393182	-1149.8541	0.084095	-1149.931212	-1150.3357
TS1_c13	-1150.2761	0.393256	-1149.8558	0.082631	-1149.932213	-1150.336177

TS1_c14	-1150.2758	0.393414	-1149.8555	0.08117	-1149.931107	-1150.336921
TS1_c15	-1150.2744	0.393397	-1149.8539	0.083686	-1149.930864	-1150.335368
TS1_c16	-1150.2761	0.393631	-1149.8556	0.081001	-1149.931111	-1150.33649
TS1_c17	-1150.2761	0.393629	-1149.8556	0.080999	-1149.931113	-1150.336484
TS1'	-1150.277	0.393093	-1149.8571	0.079533	-1149.932318	-1150.336786
TS1'_c2	-1150.2754	0.392961	-1149.8555	0.080489	-1149.931257	-1150.335812
TS1'_c3	-1150.2772	0.393357	-1149.8572	0.079086	-1149.932038	-1150.336586
TS1'_c4	-1150.2749	0.393355	-1149.8547	0.08056	-1149.93031	-1150.335835
TS1'_c5	-1150.275	0.393299	-1149.8548	0.081398	-1149.930662	-1150.335451
TS1'_c6	-1150.2744	0.392991	-1149.8546	0.080525	-1149.930179	-1150.33511
TS1'_c7	-1150.2751	0.3936	-1149.8547	0.080648	-1149.930102	-1150.335563
TS1'_c8	-1150.2751	0.393601	-1149.8547	0.080644	-1149.9301	-1150.335563
TS1'_c9	-1150.2769	0.393342	-1149.8569	0.079431	-1149.931906	-1150.335613
TS1'_c10	-1150.2761	0.393228	-1149.8562	0.078953	-1149.931066	-1150.335464
TS1'_c11	-1150.2757	0.393349	-1149.8556	0.080141	-1149.930866	-1150.33472
TS1'_c12	-1150.273	0.393368	-1149.8526	0.081397	-1149.928562	-1150.334246
TS1'_c13	-1150.2724	0.393385	-1149.852	0.081401	-1149.927849	-1150.333425
TS1'_c14	-1150.2739	0.393243	-1149.8539	0.079933	-1149.929139	-1150.333297
TS1'_c15	-1150.2729	0.393603	-1149.8524	0.080777	-1149.927904	-1150.333067
TS1'_c16	-1150.2724	0.393257	-1149.852	0.08173	-1149.928237	-1150.332206
TS1'_c17	-1150.2724	0.39332	-1149.8521	0.081529	-1149.92799	-1150.332505
TS1'_c18	-1150.2691	0.393411	-1149.8487	0.081722	-1149.924656	-1150.331706
TS1'_c19	-1150.2728	0.393208	-1149.8529	0.07951	-1149.92778	-1150.331998
TS1'_c20	-1150.3207	0.395907	-1149.8977	0.082294	-1149.974118	-1150.377395
INT2	-1150.3319	0.395984	-1149.9085	0.085376	-1149.986308	-1150.393933
INT2_c2	-1150.3319	0.396	-1149.9085	0.084812	-1149.986025	-1150.393929
INT2_c3	-1150.3338	0.39587	-1149.9105	0.083813	-1149.987578	-1150.393673
INT2_c4	-1150.333	0.395869	-1149.9098	0.084031	-1149.986989	-1150.393208
INT2_c5	-1150.3319	0.395965	-1149.9094	0.08097	-1149.984512	-1150.393937
INT2_c6	-1150.3348	0.396446	-1149.9113	0.081752	-1149.987238	-1150.393877
INT2_c7	-1150.3331	0.396494	-1149.9095	0.081989	-1149.98572	-1150.393681
INT2_c8	-1150.335	0.396326	-1149.9115	0.082536	-1149.988012	-1150.393246
INT2_c9	-1150.3334	0.396357	-1149.9098	0.083075	-1149.98643	-1150.393096

INT2_c10	-1150.3334	0.396357	-1149.9098	0.083089	-1149.986436	-1150.393068
INT2_c11	-1150.3336	0.396406	-1149.9099	0.083338	-1149.986666	-1150.392856
INT2_c12	-1150.3349	0.396601	-1149.9113	0.081487	-1149.987218	-1150.39365
INT2_c13	-1150.3345	0.396587	-1149.9108	0.081552	-1149.986863	-1150.393266
INT2_c14	-1150.3345	0.39639	-1149.9109	0.082667	-1149.987503	-1150.392511
INT2_c15	-1150.3333	0.396426	-1149.9097	0.082443	-1149.986177	-1150.391986
INT2_c16	-1150.3358	0.396598	-1149.9123	0.080763	-1149.987834	-1150.392347
INT2_c17	-1150.3328	0.396595	-1149.9091	0.081986	-1149.985202	-1150.391772
INT2_c18	-1150.3328	0.396595	-1149.9091	0.081983	-1149.985201	-1150.39177
INT2_c19	-1150.3328	0.396595	-1149.9091	0.081982	-1149.9852	-1150.39177
INT2_c20	-1150.333	0.395858	-1149.9098	0.082735	-1149.986457	-1150.390447
INT2'	-1150.3271	0.395611	-1149.9042	0.083694	-1149.981292	-1150.390396
INT2'_c2	-1150.3287	0.396032	-1149.9055	0.082125	-1149.981971	-1150.39121
INT2'_c3	-1150.3289	0.396058	-1149.9058	0.082313	-1149.982176	-1150.391002
INT2'_c4	-1150.3296	0.396291	-1149.9063	0.081437	-1149.982312	-1150.391251
INT2'_c5	-1150.3301	0.396154	-1149.9069	0.081941	-1149.983105	-1150.390921
INT2'_c6	-1150.3305	0.39628	-1149.9073	0.080999	-1149.983015	-1150.391068
INT2'_c7	-1150.3305	0.396479	-1149.9071	0.080694	-1149.982686	-1150.391351
INT2'_c8	-1150.3305	0.39648	-1149.9071	0.080689	-1149.982683	-1150.391352
INT2'_c9	-1150.3274	0.396	-1149.9042	0.082739	-1149.981009	-1150.389648
INT2'_c10	-1150.3278	0.395752	-1149.9048	0.082054	-1149.981215	-1150.389353
INT2'_c11	-1150.3272	0.395872	-1149.9039	0.083814	-1149.981299	-1150.388538
INT2'_c12	-1150.3273	0.395857	-1149.904	0.083357	-1149.981233	-1150.388441
INT2'_c13	-1150.3286	0.395676	-1149.9056	0.083072	-1149.982552	-1150.38812
INT2'_c14	-1150.3276	0.395928	-1149.9045	0.082873	-1149.981344	-1150.388122
INT2'_c15	-1150.328	0.396002	-1149.9049	0.081938	-1149.981238	-1150.388399
INT2'_c16	-1150.328	0.396003	-1149.9049	0.081939	-1149.981237	-1150.388398
INT2'_c17	-1150.328	0.396004	-1149.9049	0.081932	-1149.981233	-1150.3884
INT2'_c18	-1150.328	0.396003	-1149.9049	0.08194	-1149.981237	-1150.388396
INT2'_c19	-1150.3268	0.39593	-1149.9036	0.082212	-1149.980077	-1150.386844
INT2'_c20	-1150.3289	0.396485	-1149.9055	0.079987	-1149.980976	-1150.387847
TS2a	-1150.2788	0.393432	-1149.8583	0.082563	-1149.934589	-1150.340712
TS2a_c2	-1150.2785	0.393549	-1149.8579	0.082262	-1149.934068	-1150.340112

TS2a_c3	-1150.2787	0.393555	-1149.8581	0.082042	-1149.9342	-1150.340019
TS2a_c4	-1150.2799	0.39361	-1149.8594	0.080954	-1149.935026	-1150.340329
TS2a_c5	-1150.2782	0.393583	-1149.8576	0.081918	-1149.933536	-1150.339832
TS2a_c6	-1150.278	0.393341	-1149.8575	0.082624	-1149.933893	-1150.339256
TS2a_c7	-1150.2782	0.393281	-1149.8577	0.082853	-1149.934348	-1150.338913
TS2a_c8	-1150.279	0.393658	-1149.8585	0.081687	-1149.934253	-1150.339818
TS2a_c9	-1150.2781	0.393354	-1149.8576	0.082803	-1149.934158	-1150.338916
TS2a_c10	-1150.2776	0.393581	-1149.857	0.082512	-1149.933257	-1150.338904
TS2a_c11	-1150.2792	0.393658	-1149.8587	0.0808	-1149.934187	-1150.339335
TS2a_c12	-1150.2774	0.39342	-1149.8569	0.08244	-1149.933099	-1150.338533
TS2a_c13	-1150.2783	0.393622	-1149.8577	0.081796	-1149.933566	-1150.338647
TS2a_c14	-1150.2769	0.393056	-1149.8565	0.083148	-1149.933308	-1150.337498
TS2a_c15	-1150.2799	0.393894	-1149.8593	0.079818	-1149.934233	-1150.339429
TS2a_c16	-1150.2777	0.393412	-1149.8574	0.081083	-1149.933089	-1150.33786
TS2a_c17	-1150.2789	0.393663	-1149.8583	0.081598	-1149.934216	-1150.337755
TS2a_c18	-1150.2768	0.393552	-1149.8563	0.081306	-1149.931963	-1150.33771
TS2a_c19	-1150.2801	0.393885	-1149.8596	0.07981	-1149.934442	-1150.337841
TS2a_c20	-1150.2784	0.393621	-1149.858	0.080804	-1149.933343	-1150.33639
TS2b	-1150.2797	0.393385	-1149.8596	0.080076	-1149.934771	-1150.338496
TS2b_c2	-1150.2778	0.393669	-1149.8573	0.082125	-1149.933183	-1150.337204
TS2b_c3	-1150.2778	0.39367	-1149.8573	0.08212	-1149.93318	-1150.337204
TS2b_c4	-1150.2778	0.393673	-1149.8573	0.082109	-1149.933174	-1150.337204
TS2b_c5	-1150.2778	0.393672	-1149.8573	0.082109	-1149.933174	-1150.337204
TS2b_c6	-1150.2796	0.393416	-1149.8595	0.079716	-1149.934381	-1150.337641
TS2b_c7	-1150.2771	0.393519	-1149.8567	0.082105	-1149.932655	-1150.336601
TS2b_c8	-1150.2764	0.393477	-1149.8559	0.082627	-1149.932144	-1150.336289
TS2b_c9	-1150.2764	0.393476	-1149.8559	0.082627	-1149.932144	-1150.336289
TS2b_c10	-1150.2775	0.393558	-1149.8571	0.08211	-1149.933075	-1150.336407
TS2b_c11	-1150.2775	0.393558	-1149.8571	0.082106	-1149.933073	-1150.336407
TS2b_c12	-1150.2775	0.393558	-1149.8571	0.082105	-1149.933072	-1150.336407
TS2b_c13	-1150.2781	0.393354	-1149.858	0.079885	-1149.933013	-1150.336448
TS2b_c14	-1150.2779	0.393868	-1149.8574	0.079911	-1149.932328	-1150.336871
TS2b_c15	-1150.2759	0.393686	-1149.8554	0.082007	-1149.931316	-1150.335155

TS2b_c16	-1150.2779	0.39367	-1149.8576	0.080179	-1149.932678	-1150.335317
TS2b_c17	-1150.2771	0.394053	-1149.8563	0.080183	-1149.931395	-1150.335645
TS2b_c18	-1150.2756	0.393729	-1149.8549	0.081246	-1149.930588	-1150.334871
TS2b_c19	-1150.278	0.393338	-1149.8581	0.078637	-1149.932622	-1150.334514
TS2b_c20	-1150.278	0.393338	-1149.8581	0.078633	-1149.93262	-1150.334514
TS2a'	-1150.2739	0.39301	-1149.8539	0.081813	-1149.930022	-1150.337612
TS2a'_c2	-1150.2739	0.393011	-1149.8539	0.081811	-1149.93002	-1150.337608
TS2a'_c3	-1150.2739	0.393011	-1149.8539	0.081812	-1149.93002	-1150.337608
TS2a'_c4	-1150.2739	0.393012	-1149.8539	0.081803	-1149.930017	-1150.337606
TS2a'_c5	-1150.2733	0.393202	-1149.853	0.081616	-1149.929027	-1150.337503
TS2a'_c6	-1150.2747	0.393387	-1149.8545	0.08141	-1149.930266	-1150.337441
TS2a'_c7	-1150.2744	0.393388	-1149.8542	0.081681	-1149.930064	-1150.337326
TS2a'_c8	-1150.2746	0.393248	-1149.8544	0.081334	-1149.930311	-1150.337067
TS2a'_c9	-1150.2759	0.393572	-1149.8556	0.080702	-1149.930978	-1150.33753
TS2a'_c10	-1150.2745	0.393291	-1149.8543	0.080662	-1149.929966	-1150.337017
TS2a'_c11	-1150.2744	0.393626	-1149.854	0.080131	-1149.929231	-1150.337584
TS2a'_c12	-1150.2744	0.393624	-1149.854	0.080135	-1149.929234	-1150.337567
TS2a'_c13	-1150.2738	0.393313	-1149.8536	0.080672	-1149.929193	-1150.336951
TS2a'_c14	-1150.2727	0.39358	-1149.8522	0.080682	-1149.927753	-1150.336696
TS2a'_c15	-1150.2729	0.393488	-1149.8526	0.080283	-1149.927997	-1150.336134
TS2a'_c16	-1150.2717	0.39312	-1149.8515	0.083073	-1149.928088	-1150.33458
TS2a'_c17	-1150.27	0.393178	-1149.8498	0.081995	-1149.925875	-1150.334843
TS2a'_c18	-1150.2712	0.39305	-1149.8511	0.081544	-1149.926964	-1150.332731
TS2a'_c19	-1150.2712	0.39305	-1149.8511	0.081541	-1149.926964	-1150.33273
TS2a'_c20	-1150.2712	0.393053	-1149.8511	0.08153	-1149.926957	-1150.33273
TS2b'	-1150.2727	0.393111	-1149.8525	0.083418	-1149.929295	-1150.333969
TS2b'_c2	-1150.2744	0.393808	-1149.8539	0.080469	-1149.929155	-1150.335147
TS2b'_c3	-1150.2747	0.393269	-1149.8548	0.079316	-1149.929683	-1150.334933
TS2b'_c4	-1150.2714	0.393253	-1149.8511	0.082865	-1149.92754	-1150.333661
TS2b'_c5	-1150.2737	0.393426	-1149.8534	0.081331	-1149.929165	-1150.334208
TS2b'_c6	-1150.2726	0.393175	-1149.8524	0.082435	-1149.928732	-1150.333424
TS2b'_c7	-1150.2742	0.393177	-1149.8542	0.080107	-1149.929512	-1150.333229
TS2b'_c8	-1150.2688	0.392963	-1149.8488	0.08371	-1149.925739	-1150.331315

TS2b'_c9	-1150.2691	0.393385	-1149.8487	0.082464	-1149.924906	-1150.33131
TS2b'_c10	-1150.2705	0.393598	-1149.85	0.080692	-1149.925592	-1150.331755
TS2b'_c11	-1150.2679	0.393392	-1149.8475	0.082383	-1149.923669	-1150.330738
TS2b'_c12	-1150.2729	0.394042	-1149.8523	0.078559	-1149.926773	-1150.332517
TS2b'_c13	-1150.2726	0.393916	-1149.852	0.079383	-1149.926966	-1150.332076
TS2b'_c14	-1150.2693	0.393743	-1149.8488	0.079856	-1149.923926	-1150.330997
TS2b'_c15	-1150.2693	0.393746	-1149.8488	0.079848	-1149.92392	-1150.330996
TS2b'_c16	-1150.2693	0.393747	-1149.8488	0.079846	-1149.923919	-1150.330997
TS2b'_c17	-1150.2693	0.393748	-1149.8488	0.079842	-1149.923917	-1150.330998
TS2b'_c18	-1150.2693	0.393749	-1149.8488	0.079837	-1149.923914	-1150.330998
TS2b'_c19	-1150.2693	0.39375	-1149.8488	0.079835	-1149.923912	-1150.330999
TS2b'_c20	-1150.2689	0.393474	-1149.8485	0.081093	-1149.924217	-1150.330188
INT3	-1150.3285	0.392765	-1149.9068	0.087888	-1149.987675	-1150.392516
INT3_c2	-1150.3322	0.393079	-1149.9103	0.087441	-1149.990814	-1150.391628
INT3_c3	-1150.3324	0.393213	-1149.9104	0.086925	-1149.990614	-1150.391823
INT3_c4	-1150.3329	0.393282	-1149.911	0.086246	-1149.990871	-1150.391921
INT3_c5	-1150.3328	0.393326	-1149.9108	0.086275	-1149.990765	-1150.391825
INT3_c6	-1150.3328	0.393324	-1149.9108	0.086281	-1149.990769	-1150.39182
INT3_c7	-1150.3332	0.393507	-1149.9112	0.086033	-1149.990821	-1150.391564
INT3_c8	-1150.3326	0.39354	-1149.9105	0.086305	-1149.990283	-1150.391269
INT3_c9	-1150.3341	0.3937	-1149.912	0.08457	-1149.990987	-1150.391912
INT3_c10	-1150.3312	0.393854	-1149.9089	0.086301	-1149.988598	-1150.391094
INT3_c11	-1150.3319	0.393173	-1149.9101	0.086137	-1149.989875	-1150.39029
INT3_c12	-1150.3328	0.393591	-1149.9107	0.085957	-1149.99039	-1150.390638
INT3_c13	-1150.3298	0.393341	-1149.9078	0.086405	-1149.987643	-1150.389966
INT3_c14	-1150.3306	0.393572	-1149.9085	0.085029	-1149.987807	-1150.390488
INT3_c15	-1150.3306	0.393574	-1149.9085	0.085023	-1149.987803	-1150.39049
INT3_c16	-1150.3317	0.393668	-1149.9096	0.084546	-1149.988665	-1150.390311
INT3_c17	-1150.3314	0.39393	-1149.9091	0.084491	-1149.988026	-1150.389428
INT3_c18	-1150.3307	0.393924	-1149.9083	0.084787	-1149.987484	-1150.389272
INT3_c19	-1150.3307	0.393926	-1149.9083	0.084782	-1149.98748	-1150.389272
INT3_c20	-1150.3314	0.393942	-1149.9091	0.084415	-1149.987988	-1150.389433
PRD_c1	-575.15267	0.195984	-574.94254	0.052692	-574.992475	-575.1917012

Structure	E/au	ZPE/au	H/au	T.S/au	qh-G/au	SP
PRD_c2	-575.15267	0.195985	-574.94254	0.052685	-574.992472	-575.1916942
PRD_c3	-575.15224	0.196085	-574.94199	0.053313	-574.992283	-575.1908133
PRD_c4	-575.15224	0.196086	-574.94199	0.053296	-574.992274	-575.1908092
PRD_c5	-575.15089	0.195783	-574.94073	0.054104	-574.991648	-575.1900387
PRD_c6	-575.15143	0.195941	-574.94138	0.053059	-574.991502	-575.1904693
PRD_c7	-575.15143	0.195941	-574.94138	0.053053	-574.991499	-575.190469
PRD_c8	-575.15143	0.195941	-574.94138	0.053052	-574.991498	-575.1904689
PRD_c9	-575.15143	0.195941	-574.94138	0.053057	-574.9915	-575.1904663
PRD_c10	-575.15143	0.195942	-574.94138	0.053056	-574.9915	-575.1904659
PRD_c11	-575.15143	0.195941	-574.94138	0.053051	-574.991497	-575.1904677
PRD_c12	-575.15198	0.195807	-574.94201	0.053006	-574.992197	-575.1894769
PRD_c13	-575.15198	0.195808	-574.94201	0.053004	-574.992196	-575.189476
PRD_c14	-575.15375	0.196301	-574.94353	0.051012	-574.992708	-575.1897872
PRD_c15	-575.15211	0.195787	-574.94207	0.053295	-574.992608	-575.1882257
PRD_c16	-575.15211	0.195788	-574.94207	0.053293	-574.992607	-575.1882256
PRD_c17	-575.15302	0.196311	-574.94277	0.051858	-574.992142	-575.1895972
PRD_c18	-575.15302	0.196313	-574.94277	0.05185	-574.992137	-575.1895973
PRD_c19	-575.15278	0.196062	-574.94283	0.05074	-574.991878	-575.1892959
PRD_c20	-575.15278	0.196062	-574.94283	0.05074	-574.991878	-575.1892948

Benchmarking – SMD(CHCl$_3$)-M06-2X/def2-TZVP//M06-2X/def2-SVP						
Structure	**E/au**	**ZPE/au**	**H/au**	**T.S/au**	**qh-G/au**	**SP**
INT1'-4m	-1150.329	0.393618	-1149.9067	0.08598	-1149.986455	-1151.662602
TS1'-4m	-1150.2454	0.391028	-1149.8261	0.085033	-1149.905151	-1151.585289
INT2'-4m	-1150.3162	0.394549	-1149.8938	0.08464	-1149.972012	-1151.648587
INT1-4m	-1150.3243	0.393211	-1149.9021	0.088177	-1149.98295	-1151.657663
TS1-4m	-1150.2471	0.390691	-1149.8281	0.084053	-1149.906693	-1151.584067
TS2a-4m	-1150.2477	0.39169	-1149.8279	0.08523	-1149.906621	-1151.582574
INT3a-4m	-1150.3233	0.393239	-1149.9019	0.085431	-1149.980956	-1151.657972
TS2b-4m	-1150.2469	0.3922	-1149.827	0.081639	-1149.903938	-1151.579805
INT3b-4m	-1150.3126	0.393996	-1149.8899	0.085819	-1149.969792	-1151.648353
INT1-4m	-1150.3243	0.393211	-1149.9021	0.088177	-1149.98295	-1151.657663

Benchmarking – SMD(CHCl₃)-DLPNO-CCSD(T)/CBS//M06-2X/def2-SVP						
Structure	E/au	ZPE/au	H/au	T.S/au	qh-G/au	SP
INT1'-4m	-1150.329	0.393618	-1149.9067	0.08598	-1149.986455	-1150.390716
TS1'-4m	-1150.2454	0.391028	-1149.8261	0.085033	-1149.905151	-1150.312855
INT2'-4m	-1150.3162	0.394549	-1149.8938	0.08464	-1149.972012	-1150.376928
TS2b'-4m	-1150.249	0.391513	-1149.8295	0.084244	-1149.907763	-1150.315139
INT3b'-4m	-1150.3264	0.392884	-1149.9044	0.088759	-1149.98555	-1150.389108
TS2a'-4m	-1150.2333	0.390099	-1149.8146	0.087429	-1149.894822	-1150.29994
INT3a'-4m	-1150.3243	0.392503	-1149.9026	0.088233	-1149.984042	-1150.393586
INT1-4m	-1150.3243	0.393211	-1149.9021	0.088177	-1149.98295	-1150.387481
TS1-4m	-1150.2471	0.390691	-1149.8281	0.084053	-1149.906693	-1150.310898
INT2-4m	-1150.323	0.395339	-1149.8999	0.085211	-1149.977927	-1150.382758
TS2a-4m	-1150.2477	0.39169	-1149.8279	0.08523	-1149.906621	-1150.312956
INT3a-4m	-1150.3233	0.393239	-1149.9019	0.085431	-1149.980956	-1150.387781
TS2b-4m	-1150.2469	0.3922	-1149.827	0.081639	-1149.903938	-1150.307512
INT3b-4m	-1150.3126	0.393996	-1149.8899	0.085819	-1149.969792	-1150.377888
INT1'-4m	-1150.329	0.393618	-1149.9067	0.08598	-1149.986455	-1150.390716
TS1'-4m	-1150.2454	0.391028	-1149.8261	0.085033	-1149.905151	-1150.312855
INT2'-4m	-1150.3162	0.394549	-1149.8938	0.08464	-1149.972012	-1150.376928
TS2b'-4m	-1150.249	0.391513	-1149.8295	0.084244	-1149.907763	-1150.315139
INT3b'-4m	-1150.3264	0.392884	-1149.9044	0.088759	-1149.98555	-1150.389108
TS2a'-4m	-1150.2333	0.390099	-1149.8146	0.087429	-1149.894822	-1150.29994
INT3a'-4m	-1150.3243	0.392503	-1149.9026	0.088233	-1149.984042	-1150.393586
INT1-4m	-1150.3243	0.393211	-1149.9021	0.088177	-1149.98295	-1150.387481
TS1-4m	-1150.2471	0.390691	-1149.8281	0.084053	-1149.906693	-1150.310898
INT2-4m	-1150.323	0.395339	-1149.8999	0.085211	-1149.977927	-1150.382758
TS2a-4m	-1150.2477	0.39169	-1149.8279	0.08523	-1149.906621	-1150.312956
INT3a-4m	-1150.3233	0.393239	-1149.9019	0.085431	-1149.980956	-1150.387781
TS2b-4m	-1150.2469	0.3922	-1149.827	0.081639	-1149.903938	-1150.307512
INT3b-4m	-1150.3126	0.393996	-1149.8899	0.085819	-1149.969792	-1150.377888
Benchmarking – SMD(CHCl₃)-M06-2X/def2-TZVP//SMD(CHCl₃)-M06-2X/def2-SVP						

Structure	E/au	ZPE/au	H/au	T.S/au	qh-G/au	SP
MAA_solv	-535.90554	0.166733	-535.72589	0.049209	-535.77298	-536.5217086
PNA_solv	-614.42445	0.223517	-614.18512	0.057751	-614.2393	-615.131465
INT1-4m_solv	-1150.3435	0.392231	-1149.9223	0.088313	-1150.0032	-1151.658284
TS1-4m_solv	-1150.2666	0.38961	-1149.8485	0.084517	-1149.9276	-1151.585253
INT2-4m_solv	-1150.3445	0.394517	-1149.922	0.087035	-1150.0011	-1151.658282
TS2b-4m_solv	-1150.265	0.390786	-1149.8463	0.083146	-1149.9241	-1151.580547
INT3b-4m_solv	-1150.3328	0.393326	-1149.9109	0.085545	-1149.9905	-1151.648936
TS2a-4m_solv	-1150.2673	0.390401	-1149.8486	0.086109	-1149.9279	-1151.585416
INT3a-4m_solv	-1150.3432	0.392117	-1149.9218	0.089632	-1150.0035	-1151.658568
PRD_solv	-575.16337	0.19541	-574.95362	0.053838	-575.0044	-575.82498

Benchmarking – SMD(CHCl$_3$)-M06-2X/6-311++G(d,p)//M06-2X/6-31+G(d)

Structure	E/au	ZPE/au	H/au	T.S/au	qh-G/au	SP
MAA	-536.30824	0.167878	-536.12743	0.049372	-536.17456	-536.463194
PNA	-614.88502	0.225211	-614.64401	0.057987	-614.69825	-615.067343
INT1'_4m	-1151.2142	0.395513	-1150.7899	0.08655	-1150.87	-1151.54464
TS1'_4m	-1151.133	0.392953	-1150.7117	0.085756	-1150.7911	-1151.468593
INT2'_4m	-1151.2004	0.396465	-1150.776	0.085004	-1150.8544	-1151.529199
INT1_4m	-1151.2081	0.394938	-1150.7841	0.088664	-1150.8652	-1151.539029
TS1_4m	-1151.1334	0.392514	-1150.7124	0.085471	-1150.7918	-1151.466316
INT2_4m	-1151.2103	0.397318	-1150.785	0.087053	-1150.8641	-1151.537704
TS2a_4m	-1151.1347	0.393436	-1150.713	0.085758	-1150.7921	-1151.466351
INT3a_4m	-1151.2085	0.39477	-1150.7845	0.089231	-1150.866	-1151.540108
TS2b_4m	-1151.1314	0.393784	-1150.7098	0.082651	-1150.7873	-1151.462661
INT3b_4m	-1151.1975	0.395548	-1150.7731	0.087056	-1150.8537	-1151.530317

Acid catalysis

Structure	E/au	ZPE/au	H/au	T.S/au	qh-G/au	SP
TS_RCT	-1150.6876	0.403987	-1150.2542	0.092402	-1150.337338	-1150.796388

TS_acid_prime	-1150.6261	0.402294	-1150.1941	0.090672	-1150.276776	-1150.750628
TS_INT	-1150.6545	0.403093	-1150.2207	0.094493	-1150.306029	-1150.773914
TS_acid	-1150.6364	0.402793	-1150.2041	0.089929	-1150.286391	-1150.757693
TS_acid_c2	-1150.6338	0.402885	-1150.2014	0.08919	-1150.283329	-1150.756322
TS_acid_c3	-1150.6358	0.40309	-1150.2035	0.087809	-1150.284576	-1150.755819
TS_acid_c4	-1150.6348	0.403154	-1150.2024	0.087654	-1150.28354	-1150.755425
TS_acid_c5	-1150.6308	0.402955	-1150.1985	0.087669	-1150.279845	-1150.754766
TS_acid_c6	-1150.6346	0.403361	-1150.2022	0.085342	-1150.282452	-1150.755551
TS_acid_c7	-1150.6375	0.40358	-1150.2049	0.08616	-1150.285226	-1150.75555
TS_acid_c8	-1150.6351	0.403904	-1150.2023	0.085431	-1150.282287	-1150.755016
TS_acid_c9	-1150.6351	0.403903	-1150.2023	0.085432	-1150.282287	-1150.755013
TS_acid_c10	-1150.6362	0.403528	-1150.2036	0.086719	-1150.284173	-1150.753653
TS_acid_c11	-1150.6356	0.403072	-1150.2036	0.085476	-1150.28367	-1150.753441
TS_acid_c12	-1150.6332	0.403657	-1150.2005	0.085636	-1150.280716	-1150.752696

IV. Supplementary References:

Full reference Gaussian 16:

Gaussian 16, Revision B.01, Frisch, M. J.; Trucks, G. W.; Schlegel, H. B.; Scuseria, G. E.; Robb, M. A.; Cheeseman, J. R.; Scalmani, G.; Barone, V.; Mennucci, B.; Petersson, G. A.; Nakatsuji, H.; Caricato, M.; Li, X.; Hratchian, H. P.; Izmaylov, A. F.; Bloino, J.; Zheng, G.; Sonnenberg, J. L.; Hada, M.; Ehara, M.; Toyota, K.; Fukuda, R.; Hasegawa, J.; Ishida, M.; Nakajima, T.; Honda, Y.; Kitao, O.; Nakai, H.; Vreven, T.; Montgomery Jr., J. A.; Peralta, J. E.; Ogliaro, F.; Bearpark, M.; Heyd, J. J.; Brothers, E.; Kudin, K. N.; Staroverov, V. N.; Kobayashi, R.; Normand, J.; Raghavachari, K.; Rendell, A.; Burant, J. C.; Iyengar, S. S.; Tomasi, J.; Cossi, M.; Rega, N.; Millam, J. M.; Klene, M.; Knox, J. E.; Cross, J. B.; Bakken, V.; Adamo, C.; Jaramillo, J.; Gomperts, R.; Stratmann, R. E.; Yazyev, O.; Austin, A. J.; Cammi, R.; Pomelli, C.; Ochterski, J. W.; Martin, R. L.; Morokuma, K.; Zakrzewski, V. G.; Voth, G. A.; Salvador, P.; Dannenberg, J. J.; Dapprich, S.; Daniels, A. D.; Farkas, Ö.; Foresman, J. B.; Ortiz, J. V; Cioslowski, J.; Fox, D. J. Gaussian, Inc., Wallingford CT, 2016.

(1)   Zhao, Y.; Truhlar, D. G. The M06 Suite of Density Functionals for Main Group Thermochemistry, Thermochemical Kinetics, Noncovalent Interactions, Excited States, and Transition Elements: Two New Functionals and Systematic Testing of Four M06-Class Functionals and 12 Other Function. *Theor. Chem. Acc.* **2008**, *120* (1), 215–241.

(2)   Weigend, F.; Ahlrichs, R. Balanced Basis Sets of Split Valence, Triple Zeta Valence and Quadruple Zeta Valence Quality for H to Rn: Design and Assessment of Accuracy. *Phys. Chem. Chem. Phys.* **2005**, *7* (18), 3297–3305.

(3)   Weigend, F. Accurate Coulomb-Fitting Basis Sets for H to Rn. *Phys. Chem. Chem. Phys.* **2006**, *8* (9), 1057–1065.

(4)   Ditchfield, R.; Hehre, W. J.; Pople, J. A. Self-Consistent Molecular-Orbital Methods. IX. An Extended Gaussian-Type Basis for Molecular-Orbital Studies of Organic Molecules. *J. Chem. Phys.* **2004**, *54* (2), 724–728.

(5)   Marenich, A. V.; Cramer, C. J.; Truhlar, D. G. Universal Solvation Model Based on Solute Electron Density and on a Continuum Model of the Solvent Defined by the Bulk Dielectric Constant and Atomic Surface Tensions. *J. Phys. Chem. B* **2009**, *113* (18), 6378–6396.

(6)   Frisch, M. J. .; Trucks, G. W. .; Schlegel, H. B. .; Scuseria, G. E. .; Robb, M. A. .; Cheeseman, J. R. .; Scalmani, G. .; Barone, V. .; Petersson, G. A. .; Nakatsuji, H. .; et al. Gaussian 16, Revision B.01. 2016.

(7)   Riplinger, C.; Neese, F. An Efficient and near Linear Scaling Pair Natural Orbital Based Local Coupled Cluster Method. *J. Chem. Phys.* **2013**, *138* (3), 034106.

(8)   Riplinger, C.; Sandhoefer, B.; Hansen, A.; Neese, F. Natural Triple Excitations in Local Coupled Cluster Calculations with Pair Natural Orbitals. *J. Chem. Phys.* **2013**, *139* (13), 134101.

(9)   Neese, F. The ORCA Program System. *Wiley Interdiscip. Rev. Comput. Mol. Sci.* **2012**, *2* (1), 73–78.

(10)   Neese, F. Software Update: The ORCA Program System, Version 4.0. *Wiley Interdiscip. Rev. Comput. Mol. Sci.* **2018**, *8* (1), e1327.

(11)   Neese, F.; Wennmohs, F.; Becker, U.; Riplinger, C. The ORCA Quantum Chemistry Program Package. *J. Chem. Phys.* **2020**, *152* (22), 224108.

(12)   Guo, Y.; Riplinger, C.; Becker, U.; Liakos, D. G.; Minenkov, Y.; Cavallo, L.; Neese, F. An Improved Linear Scaling Perturbative Triples Correction for the Domain Based Local Pair-Natural Orbital Based Singles and Doubles Coupled Cluster Method [DLPNO-CCSD(T)]. *J. Chem. Phys.* **2018**, *148* (1), 011101.

(13)   Kollmar, C. The Role of Energy Denominators in Self-consistent Field (SCF) Calculations for Open Shell Systems. *J. Chem. Phys.* **1996**, *105* (18), 8204–8212.

(14)   Halkier, A.; Helgaker, T.; Jørgensen, P.; Klopper, W.; Koch, H.; Olsen, J.; Wilson, A. K. Basis-Set Convergence in Correlated Calculations on Ne, N 2 , and H 2 O. *Chem. Phys. Lett.* **1998**, *286* (3–4), 243–252.

(15)   Helgaker, T.; Klopper, W.; Koch, H.; Noga, J. Basis-Set Convergence of Correlated Calculations on Water. *J. Chem. Phys.* **1997**, *106* (23), 9639–9646.

(16)   Halkier, A.; Helgaker, T.; Jørgensen, P.; Klopper, W.; Olsen, J. Basis-Set Convergence of the Energy in Molecular Hartree-Fock Calculations. *Chem. Phys. Lett.* **1999**, *302* (5–6), 437–446.

(17)   Dunning, T. H. Gaussian Basis Sets for Use in Correlated Molecular Calculations. I. The Atoms Boron through Neon and Hydrogen. *J. Chem. Phys.* **1989**, *90* (2), 1007–1023.

(18)   Woon, D. E.; Dunning, T. H. Gaussian Basis Sets for Use in Correlated Molecular

Calculations. III. The Atoms Aluminum through Argon. *J. Chem. Phys.* **1993**, *98* (2), 1358–1371.

(19)   Woon, D. E.; Dunning, T. H. Gaussian Basis Sets for Use in Correlated Molecular Calculations. V. Core-valence Basis Sets for Boron through Neon. *J. Chem. Phys.* **1995**, *103* (11), 4572–4585.

(20)   Stoychev, G. L.; Auer, A. A.; Neese, F. Automatic Generation of Auxiliary Basis Sets. *J. Chem. Theory Comput.* **2017**, *13* (2), 554–562.

(21)   Schrödinger, L. *The PyMOL Molecular Graphics Development Component, Version 1.8*; 2015.

(22)   Tillman, K. R.; Meacham, R.; Highmoore, J. F.; Barankovich, M.; Witkowski, A. M.; Mather, P. T.; Graf, T.; Shipp, D. A.; Rolsma, A. N.; Barankovich, M.; et al. Dynamic Covalent Exchange in Poly(Thioether Anhydrides). *Polym. Chem.* **2020**, *11* (47), 7551–7561.

(23)   Needleman, S. B.; Wunsch, C. D. A General Method Applicable to the Search for Similarities in the Amino Acid Sequence of Two Proteins. *J. Mol. Biol.* **1970**, *48* (3), 443–453.

(24)   Henikoff, S.; Henikoff, J. G. Amino Acid Substitution Matrices from Protein Blocks. *Proc. Natl. Acad. Sci. U. S. A.* **1992**, *89* (22), 10915–10919.

(25)   Kabsch, W. A Solution for the Best Rotation to Relate Two Sets of Vectors. *Acta Cryst.* **1976**, *32* (5), 922–923.

(26)   Liakos, D. G.; Sparta, M.; Kesharwani, M. K.; Martin, J. M. L.; Neese, F. Exploring the Accuracy Limits of Local Pair Natural Orbital Coupled-Cluster Theory. *J. Chem. Theory Comput.* **2015**, *11* (4), 1525–1539.

(27)   Mallick, S.; Roy, B.; Kumar, P. A Comparison of DLPNO-CCSD(T) and CCSD(T) Method for the Determination of the Energetics of Hydrogen Atom Transfer Reactions. *Comput. Theor. Chem.* **2020**, *1187*, 112934.

(28)   Clarke, R. W.; McGraw, M. L.; Newell, B. S.; Chen, E. Y.-X. Thermomechanical Activation Achieving Orthogonal Working/Healing Conditions of Nanostructured Tri-Block Copolymer Thermosets. *Cell Reports Phys. Sci.* **2021**, *2* (7), 100483.

(29)   Pracht, P.; Bauer, C. A.; Grimme, S. Automated and Efficient Quantum Chemical Determination and Energetic Ranking of Molecular Protonation Sites. *J. Comput. Chem.* **2017**, *38* (30), 2618–2631.

(30)   Ess, D. H.; Houk, K. N. Distortion/Interaction Energy Control of 1,3-Dipolar Cycloaddition Reactivity. *J. Am. Chem. Soc.* **2007**, *129* (35), 10646–10647.

(31)   Fernández, I.; Bickelhaupt, F. M. The Activation Strain Model and Molecular Orbital Theory: Understanding and Designing Chemical Reactions. *Chem. Soc. Rev.* **2014**, *43* (14), 4953–4967.

(32)   Bickelhaupt, F. M.; Houk, K. N. Analyzing Reaction Rates with the Distortion/Interaction-Activation Strain Model. *Angew. Chem. Int. Ed.* **2017**, *56* (34), 10070–10086.